Separation and Purification Technology 332 (2024) 125771

Contents lists available at ScienceDirect

Separation and Purification Technology

journal homepage: www.elsevier.com/locate/seppur

Highly stable hybrid porous polymers containing polyhedral oligomeric silsesquioxane (POSS)/Dibenzo[g,p]chrysene and Dibenzo[b,d]thiophene units for efficient Rhodamine B dye removal

Ching-Wen Hsiao [a,1], Ahmed M. Elewa [b,1], Mohamed Gamal Mohamed [a,c,1,*], Shiao-Wei Kuo [a,d,*]

[a] Department of Materials and Optoelectronic Science, College of Semiconductor and Advanced Technology Research, Center for Functional Polymers and Supramolecular Materials, National Sun 'Yat-Sen University, Kaohsiung 804, Taiwan
[b] Department of Chemical Engineering, National Tsing Hua University, Hsinchu, 300044, Taiwan
[c] Chemistry Department, Faculty of Science, Assiut University, Assiut 71515, Egypt
[d] Department of Medicinal and Applied Chemistry, Kaohsiung Medical University, Kaohsiung 807, Taiwan

ARTICLE INFO

Editor: S Deng

Keywords:
Hybrid porous polymers
Polyhedral oligomeric silsesquioxane
Dibenzo[g,p]chrysene
Dibenzo[b,d]thiophene
Thermal stability
Dye removal

ABSTRACT

In this study, we employed the Heck reaction method to synthesize three types of hybrid porous organic/inorganic polymers (HPPs) incorporating octavinylsilsesquioxane (OVS) units. Specifically, we synthesized OVS-TBN-DBTH, OVS-TBN-THS, and OVS-TBN-$THSO_2$ HPPs by reacting OVS with different brominated organic compounds, namely, 2,7,10,15-tetrabromodibenzo[g,p]chrysene (TBN-Br_4)/2,8-dibromodibenzo[b,d]thiophene (DBTH-Br_2), TBN-Br_4/2,3,7,8-tetrabromothianthrene (THS-Br_4), and TBN-Br_4/2,3,7,8-tetrabromothianthrene-5,5,10,10-tetraoxide ($THSO_2$-Br_4). Based on thermal analysis (TGA), the onset decomposition temperatures (T_{d10}) for these HPPs were as follows: OVS-TBN-DBTH at 575 °C, OVS-TBN-THS at 313 °C, and OVS-TBN-$THSO_2$ at 490 °C. Additionally, these HPPs exhibited high char yields, with values of 83, 53, and 67 wt% for OVS-TBN-DBTH, OVS-TBN-THS, and OVS-TBN-$THSO_2$ HPPs, respectively. Furthermore, when analyzed using nitrogen adsorption–desorption measurements, both OVS-TBN-DBTH and OVS-TBN-$THSO_2$ HPPs demonstrated impressive specific surface areas (S_{BET}) of up to 380 m^2/g. In addition, the OVS-TBN-DBTH and OVS-TBN-$THSO_2$ HPPs provide an adsorption capacity of 70.62 and 77.1 mg g^{-1} (q_{max} from Langmuir isothermal Mode) toward RhB dyestuff at room temperature. In this adsorption system, after calculation, the OVS-TBN-THS HPP could be inferred that the adsorption is a pseudo-first order adsorption model. The OVS-TBN-THS HPP and OVS-TBN-$THSO_2$ HPP in the pseudo-secondary order model have a better representation of the adsorption system for rhodamine B. This study introduces an innovative method for developing HPPs as adsorbents for water treatment and purification.

1. Introduction

Industrial wastewater has become a pervasive threat in numerous countries, presenting a widespread risk of environmental pollution [1–5]. Various organic contaminants find their way into water systems through multiple channels. The introduction of organic contaminants into natural water bodies poses a significant environmental threat, causing adverse effects on both aquatic ecosystems and human well-being [6–8]. Among these contaminants, dyes, which encompass a range of organic chemicals, present notable challenges due to their extensive application in various industries such as textiles, pharmaceuticals, plastic manufacturing, and the production of paints [9,10]. The release of toxic and deeply colored wastewater containing these dyes into aquatic environments is a major contributor to environmental pollution [9,10].

Rhodamine B (RhB) is a widely used dye in multiple sectors, including textiles and clothing, leather, and food processing [11–13]. However, this pigment is notorious for its significant toxicity, known to have carcinogenic and mutagenic properties, posing a threat to various life forms. It's worth highlighting that RhB presents a substantial and enduring risk to aquatic ecosystems, particularly concerning the health of plant organisms [11–13]. Its impact includes obstructing light

* Corresponding authors.
E-mail addresses: mgamal.eldin12@yahoo.com (M.G. Mohamed), kuosw@faculty.nsysu.edu.tw (S.-W. Kuo).
[1] These two authors contributed equally.

https://doi.org/10.1016/j.seppur.2023.125771
Received 12 October 2023; Received in revised form 11 November 2023; Accepted 16 November 2023
Available online 22 November 2023

penetration and subsequently reducing photosynthesis, disrupting natural purification processes. Thus, the complete removal of RhB from industrial wastewater is imperative to mitigate its adverse environmental effects. Various conventional methods have been employed for the removal of color molecules in wastewater, such as reverse osmosis, filtration, photodegradation, sedimentation, and coagulation, as well as adsorption techniques [14–20].

Nevertheless, many of these approaches have their limitations, including low removal efficiencies when dealing with non-biodegradable and resistant organic dyes, as well as the need for extended treatment durations and subsequent processing steps. Among the available methods, adsorption has emerged as the most effective means of eliminating dyes from wastewater. Its appeal lies in its simplicity, adaptability, cost-effectiveness, and high efficiency. Consequently, a range of adsorbent materials have been harnessed for dye removal from water-based solutions, encompassing clays [21], activated carbons[22,23], biomaterials, and metal oxides [24]. Notably, several organic polymers have recently surfaced as effective organic adsorbents for removing dyes from aqueous solutions [25–28].

Cage silsesquioxanes (SQs), often in the cubic $R_8Si_8O_{12}$ configuration, are highly coveted as structural elements for porous crafting materials due to their rigidity, strong functionalization capabilities, and remarkable resistance to heat and water. These SQ units offer the advantage of excellent thermal stability (inorganic) and the potential for further functionalization (organic) by incorporating both inorganic and organic components [29–40]. Among the numerous derivatives of cage silsesquioxanes (SQs), octavinylsilsesquioxane (OVS) shines as an exceptionally versatile monomer. OVS presents a superb choice for manufacturing porous materials through a range of synthetic methods, such as click reactions, hydrosilylation, Friedel-Crafts processes, and Heck reactions [41–51]. What adds to its appeal is the ease of accessibility and affordability of OVS. OVS stands out as the perfect starting material for crafting hybrid polymers, thanks to its unique attributes. These materials inherit outstanding optical and electrical characteristics from OVS, which also enables the adjustment of their energy gap [52,53]. Furthermore, OVS is exceptionally suitable for large-scale production due to its cost-effectiveness [52,53]. Organic and inorganic OVS have garnered growing interest as versatile building blocks for creating porous materials, thanks to their substantial rigidity and extensive functionalization. OVS-based porous organic polymers (POPs) have shown exceptional properties such as surface area, pore size, thermal stability, and electrochemical performance [54–60].

As far as our current understanding goes, there is a limited number of reports available regarding the utilization of octavinylsilsesquioxane (OVS) materials for the purpose of dye removal. In this study, considering the potentially dangerous characteristics and adverse impacts, Rhodamine B was removed from wastewater through the utilization of hybrid porous particles (HPPs) incorporating OVS nanoparticles. We synthesized three different HPPs, namely OVS-TBN-DBTH, OVS-TBN-THS, and OVS-TBN-$THSO_2$, through Heck coupling reactions. These reactions involved OVS and various brominated organic compounds (TBN-Br_4/DBTH-Br_2, TBN-Br_4/THS-Br_4, and TBN-Br_4/$THSO_2$-Br_4) in the presence of K_2CO_3 and $Pd(PPh_3)_4$ in DMF at 110 °C for 72 h (as depicted in Fig. 1**(a-c)**. To investigate the attributes of OVS-HPP materials, a variety of analytical techniques were employed, encompassing FTIR, solid-state NMR, TGA, SEM, TEM, and BET analyses. Based on TGA, T_{d10} for OVS-TBN-DBTH, OVS-TBN-THS, and OVS-TBN-$THSO_2$ HPPs were found to be 575, 313, and 490 °C. Both OVS-TBN-DBTH and OVS-TBN-$THSO_2$ HPPs exhibited remarkable S_{BET} that reached up to 380 m^2/g. Due to their favorable surface area and pore size characteristics, The HPPs, OVS-TBN-DBTH, OVS-TBN-THS, and OVS-TBN-$THSO_2$, have proven to be efficient in the removal of RhB from aqueous solutions.

2. Experimental section

2.1. Materials

Bromine solution (Br_2, 99.5 %), glacial acetic acid (AcOH, 99.7 %), $Pd(PPh_3)_4$ (99 %), *m*-chloroperoxybenzoic acid (m-CPBA, 77 %) nitromethane (CH_3NO_2), benzophenone (99 %), zinc powder (Zn, 99.99 %), titanium chloride ($TiCl_4$), dichloromethane (DCM), benzo[b,d]thiophene (DBTH), iron(III) chloride ($FeCl_3$, 97 %), thianthrene (THS, 97 %), and potassium carbonate (K_2CO_3, 99 %) were purchased from Sigma–Aldrich. Tetraphenylethene (TPE) and tetrakis(4-bromophenyl) ethylene (TPE-Br_4) were synthesized using the methods previously described [61–67]. synthesis of 2,8-dibromodibenzo[b,d]thiophene

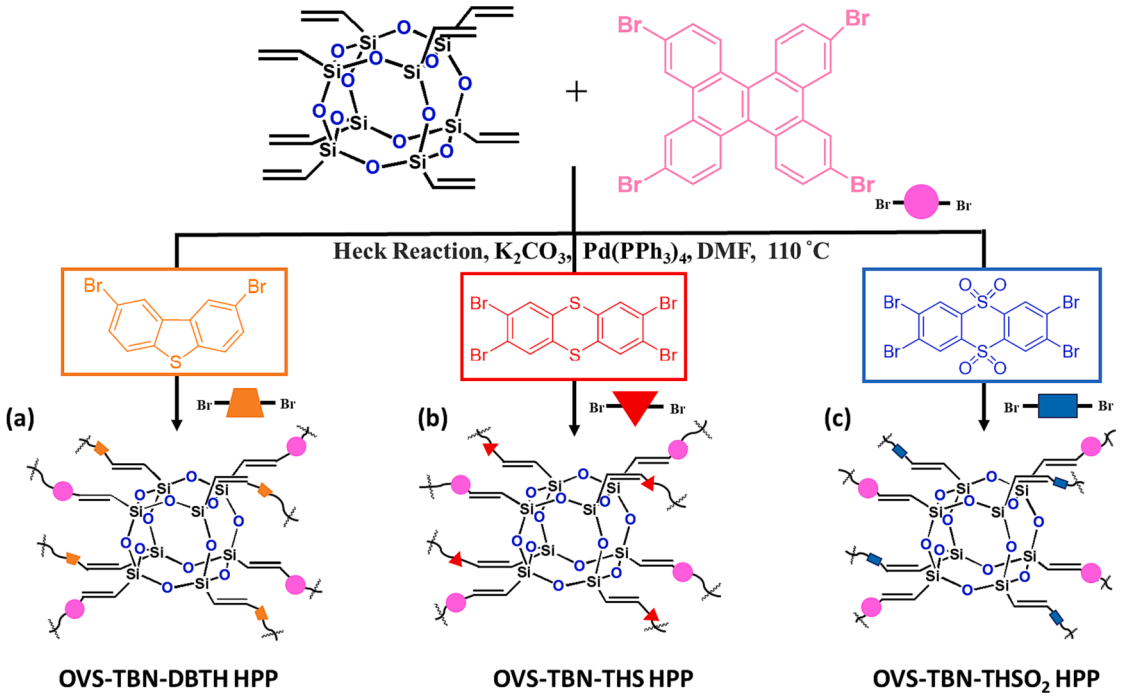

Fig. 1. Using Heck reaction to prepare (a) OVS-TBN-DBTH, (b) OVS-TBN-THS, and (c) OVS-TBN-$THSO_2$ HPPs.

(DBTH-Br_2), 2,3,7,8-tetrabromothianthrene (THS-Br_4), 2,3,7,8-tetrabromothianthrene 5,5,10,10-tetraoxide ($THSO_2$-Br_4) and 2,7,10,15-tetrabromodibenzo[g,p]chrysene (TBN-Br_4) was discussed in the detail in the Supporting information with their spectroscopic analyses [**Scheme S1-S4 and Figures S1-S9**].

2.2. Synthesis of OVS-TBN-DBTH HPP

In a dry one-neck flask, a mixture of OVS (0.3 g), TBN-Br_4 (30.6 mg), DBTH-Br_2 (0.62 g), K_2CO_3 (1.05 g), and $Pd(PPh_3)_4$ (29.6 mg). To this mixture, 20 mL of DMF was added. For three days, the resultant reaction solution was agitated at 110 °C in a nitrogen environment. After cooling the solution back to room temperature, the precipitate present in the solution was separated through a series of filtration steps, using THF, water, MeOH, and acetone as washing agents. The purification procedure resulted in the separation of OVS-TBN-DBTH HPP in the form of a yellow powder. FTIR [Fig. 2**(a)**]: 1604 (C = C stretching), and 3061 (C = C–H stretching).

2.3. Synthesis of OVS-TBN-THS HPP

In a dry one-neck flask, a mixture of OVS (0.3 g), TBN-Br_4 (30.6 mg), THS-Br_4 (0.96 g), K_2CO_3 (1.05 g), DMF (20 mL), and $Pd(PPh_3)_4$ (29.6 mg). For three days, the resultant reaction solution was agitated at 110 °C in a nitrogen environment. After cooling the solution back to room temperature, the precipitate present in the solution was separated through a series of filtration steps, using THF, water, MeOH, and acetone as washing agents. This purification process led to the isolation of OVS-TBN-THS HPP as a yellow powder. FTIR [Fig. 2**(b)**]:1605 (C = C stretching). 3062 (C = C–H stretching).

2.4. Synthesis of OVS-TBN-$THSO_2$ HPP

In a dry one-neck flask, a mixture of OVS (0.3 g), TBN-Br_4 (30.6 mg), $THSO_2$-Br_4 (1.07 g), K_2CO_3 (1.05 g), and $Pd(PPh_3)_4$ (29.6 mg). To this mixture, 20 mL of DMF was added. The resulting reaction solution was stirred at 110 °C for three days under a nitrogen atmosphere. After cooling the solution back to room temperature, the precipitate present in the solution was separated through a series of filtration steps, using THF, water, MeOH, and acetone as washing agents. This purification process led to the isolation of OVS-TBN-$THSO_2$ HPP in yellow-green power. FTIR [Fig. 2**(c)**]: 1604 (C = C stretching). 3064 (C = C–H stretching).

3. Results and discussion

3.1. Characterization of OVS-TBN-DBTH, OVS-TBN-THS, and OVS-TBN-$THSO_2$ HPPs

In this work, we delineate the synthesis procedure for three distinct types of hybrid porous polymers (HPPs), specifically OVS-TBN-DBTH, OVS-TBN-THS, and OVS-TBN-$THSO_2$ HPPs, as depicted in Fig. 1. The synthesis process involves the preparation of building block monomers, which include DBTH-Br_2, THS-Br_4, $THSO_2$-Br_4, and TBN-Br_4. DBTH-Br_2 was created by reacting Br_2 with the DBTH monomer in AcOH as the solvent [**Scheme S1**]. This reaction resulted in the formation of a white solid product. THS-Br_4 was prepared by reacting THS molecules with an excess of Br_2 in AcOH, leading to the formation of a white solid product [**Scheme S2**]. Conversion of THS-Br_4 to $THSO_2$-Br_4 [**Scheme S3**]: THS-Br_2 was subsequently subjected to a reaction with m-CPBA in DCM at 40 °C, resulting in the desired $THSO_2$-Br_4 product. TBN-Br_4 was synthesized by reacting TPE-Br_4 with a combination of $FeCl_3$ and CH_3NO_2 in DCM,

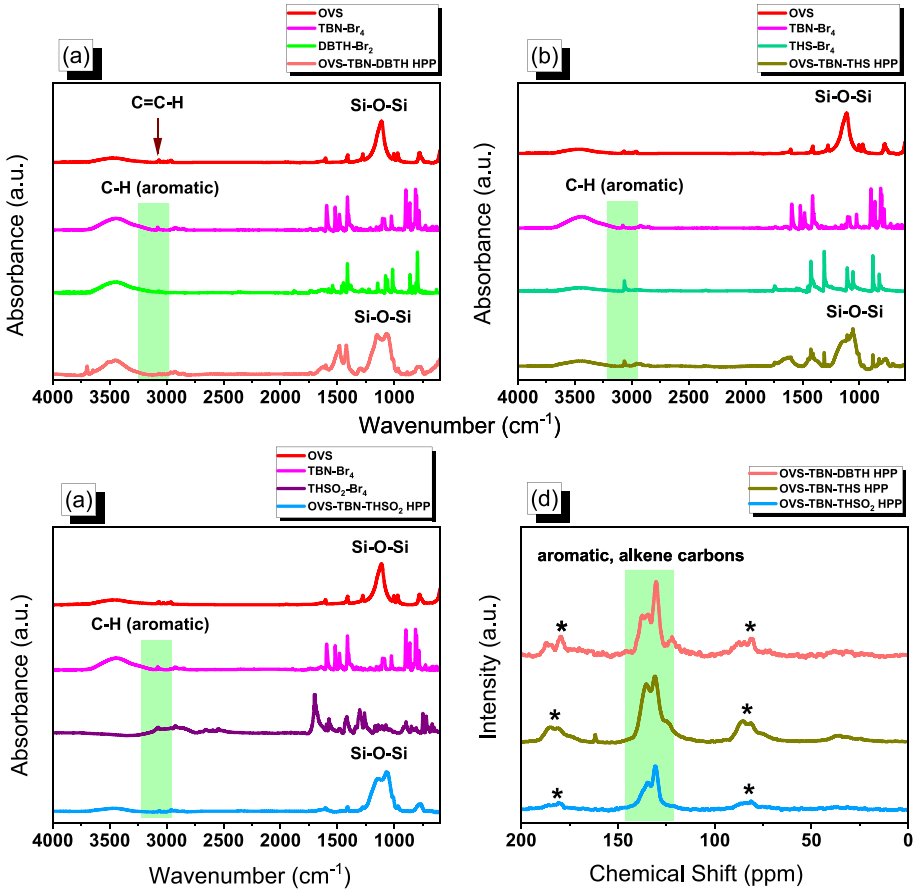

Fig. 2. FTIR profiles of (a) OVS, TBN-Br_4, DBTH-Br_2 and OVS-TBN-DBTH HPP, (b) FTIR profiles of (a) OVS, TBN-Br_4, THS-Br_2 and OVS-TBN-THS HPP, and (c) OVS, TBN-Br_4, $THSO_2$-Br_2 and OVS-TBN-$THSO_2$ HPP. Solid-state C CP/MAS NMR s spectra of OVS-TBN-DBTH, OVS-TBN-THS, and OVS-TBN-$THSO_2$ HPPs.

leading to the formation of a white powder of TBN-Br_4 [Scheme S4]. To create OVS-TBN-DBTH, OVS-TBN-THS, and OVS-TBN-$THSO_2$ HPPs, a Heck coupling reaction was employed. This reaction involved the use of TBN-Br_4/DBTH-Br_2, TBN-Br_4/THS-Br_4, and TBN-Br_4/$THSO_2$-Br_4 as starting materials, with OVS as the partner molecule. As shown in Fig. 1, the Heck reaction took place at 110 °C in DMF with K_2CO_3 and Pd $(PPh_3)_4$ acting as a catalyst.

In the experimental section and supporting information, comprehensive spectroscopic analyses, including FTIR and NMR analyses, have been provided for the synthesized TBN-Br_4, DBTH-Br_2, THS-Br_4, and $THSO_2$-Br_4 compounds. **Figure S2 and Figure S3** display the recorded ^1H and ^{13}C NMR spectra of DBTH-Br_2 in DMSO-d_6. In the ^1H NMR spectrum of DBTH-Br_2 (**Figure S2**), distinct signals were observed at chemical shifts of 8.76, 8.02, and 7.71 ppm, corresponding to the protons in the aromatic rings. This observation was further confirmed by the ^{13}C NMR spectrum shown in **Figure S3**, which exhibited prominent peaks at 139.08, 136.79, 131.14, 126.04, 125.72, and 118.92 ppm, also corresponding to the carbon atoms within the aromatic rings. The signals at 8.01 and 8.04 ppm are indicative of aromatic rings in both THS-Br_4 [**Figure S6**] and $THSO_2$-Br_4 [**Figure S7**]. In Fig. 2**(a)**, the FTIR spectra of OVS exhibited distinctive absorption peaks associated with different functional groups. Specifically, absorption peaks were detected at 1108 cm^{-1} for Si-O-Si, at 1600 cm^{-1} for C = C, and at 3065 cm^{-1} for C = C–H units. Furthermore, Fig. 2**(a)** displayed the FTIR spectrum of TBN-Br_4, which showed characteristic peaks at 1594 cm^{-1} for C = C stretching and 3078 cm^{-1} for C–H aromatic vibrations. In the case of DBTH-Br_2, THS-Br_4, and $THSO_2$-Br_4 (Fig. 2**(a), 2(b), and 2(c)** respectively), the C–H aromatic absorption peaks were observed in the range of 3064 to 3057 cm^{-1}, and the C = C stretching vibrations were prominent at 1550 cm^{-1}. Following the Heck coupling reaction, as expected, the FTIR spectra of OVS-TBN-DBTH, OVS-TBN-THS, and OVS-TBN-$THSO_2$ HPPs (Fig. 2**(a), 2(b), and 2(c)**) exhibited absorption bands in the range of 1590 to 1550 cm^{-1} for C = C stretching vibrations and 3064 to 3070 cm^{-1} for C = C–H. Additionally, the Si-O-Si absorption peak in these spectra appeared broader compared to OVS, indicating the formation of cross-linked networks as a result of the reaction [44,45,51]. In Fig. 2**(d)**, significant signals, which corresponded to the carbon resonance within the aromatic units, were identified in the ^{13}C solid-state NMR spectra of the HPPs OVS-TBN-DBTH, OVS-TBN-THS, and OVS-TBN-$THSO_2$. The range in which these signals were seen was 142–125 ppm for OVS-TBN-DBTH, 142–119 ppm for OVS-TBN-THS, and 147–125 ppm for OVS-TBN-$THSO_2$ HPPs.

Confirmation of the OVS cage within OVS-TBN-DBTH, OVS-TBN-THS, and OVS-TBN-$THSO_2$ HPPs was achieved using ^{29}Si NMR. In Fig. 3 **(a)**, a distinctive peak corresponding to Si-C = C was observed at −15.9 ppm. The T_3 (Tn: $CSi(OSi)_n(OH)_{3-n}$) signals in the NMR spectra for OVS-TBN-DBTH, OVS-TBN-THS, and OVS-TBN-$THSO_2$ HPPs were found at −83.73, −82.11, and −83.47 ppm, respectively. Notably, the absence of T_2 signals in all three synthesized HPPs indicated that the OVS cage framework remained intact within these materials. Collectively, the spectroscopic results provided compelling evidence for the successful synthesis of OVS-TBN-DBTH, OVS-TBN-THS, and OVS-TBN-$THSO_2$ HPPs, confirming the framework structure of these materials. Thermal analysis of the samples was conducted using TGA to assess the thermal properties of the synthesized monomers, OVS-TBN-DBTH, OVS-TBN-THS, and OVS-TBN-$THSO_2$ HPPs (as depicted in Fig. 3**(b-d)**). The TGA results depicted in Fig. 3**(b-d)** reveal that these HPPs exhibited enhanced thermal stability compared to OVS, TBN-Br_4, DBTH-Br_2, THS-Br_4, and $THSO_2$-Br_4. This improvement in the thermal stability of OVS-TBN-DBTH, OVS-TBN-THS, and OVS-TBN-$THSO_2$ HPPs can be attributed to the cross-linking structures within the HPPs. Among the HPP materials, OVS-TBN-DBTH HPP demonstrated the highest thermal stability. It exhibited thermal degradation temperatures (T_{d5} and T_{d10}) of 507 °C and 575 °C, respectively, along with a char yield of 83 wt%. For a comprehensive summary of T_{d5}, Td_{10}, and char yield values for OVS, TBN-Br_4, DBTH-Br_2, THS-Br_4, $THSO_2$-Br_4, OVS-TBN-DBTH, OVS-TBN-THS, and OVS-TBN-$THSO_2$ HPPs [Table S1].

The S_{BET}, V_{total}, and pore size distribution, along with additional data

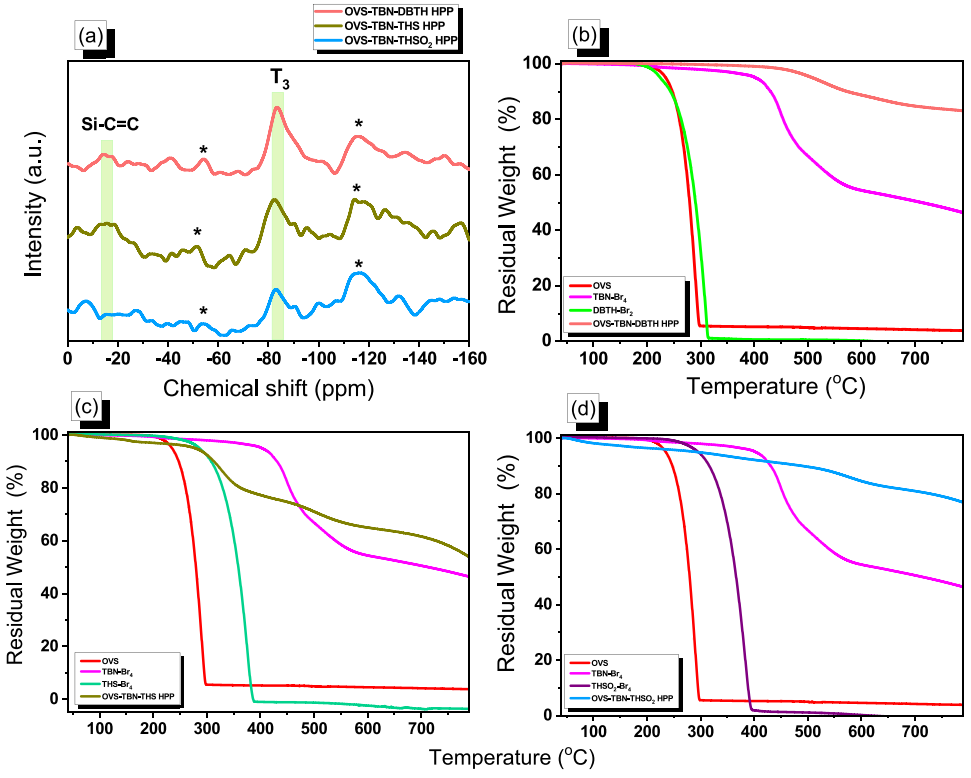

Fig. 3. solid state ^{29}Si MAS NMR of (a) OVS-TBN-DBTH, OVS-TBN-THS, and OVS-TBN-$THSO_2$ HPPs. TGA profiles of (b) OVS, TBN-Br_4, DBTH-Br_2 and OVS-TBN-DBTH HPP, (c) OVS, TBN-Br_4, THS-Br_2 and OVS-TBN-THS HPP, and (d) OVS, TBN-Br_4, $THSO_2$-Br_2 and OVS-TBN-$THSO_2$ HPP.

for OVS-TBN-DBTH, OVS-TBN-THS, and OVS-TBN-THSO$_2$ HPPs, were determined through nitrogen (N_2) adsorption/desorption measurements conducted at 77 K and 1 bar, as presented in Fig. 4**(a-f)** and **Table S2**. Prior to the BET analysis, each of the three samples underwent an 8-hour vacuum degassing process. Fig. 4**(a-c)** show that, in accordance with the IUPAC classification, the adsorption isotherms for OVS-TBN-DBTH, OVS-TBN-THS, and OVS-TBN-THSO$_2$ HPPs are categorized as type I isotherms. Among these, OVS-TBN-DBTH HPP exhibited the highest surface area, measuring 387 m^2/g, while OVS-TBN-THS HPP displayed the lowest surface area at 75 m^2/g. The S_{BET} of

OVS-TBN-THSO$_2$ HPP was found to be 381 m^2/g. Fig. 4**(d-e)** reveal that the pore sizes for OVS-TBN-DBTH and OVS-TBN-THS fall within the range of 2.24 to 9.43 nm and 2.28 to 9.43 nm, respectively. In contrast, OVS-TBN-THSO$_2$ HPP displayed a broader pore size distribution, ranging from 1.88 to 9.43 nm, indicating the presence of micropores to mesopores in its structure. Regarding V_{total}, OVS-TBN-DBTH HPP exhibited the highest value at 1.22 $cm^3\ g^{-1}$, surpassing the other two HPPs, with OVS-TBN-THSO$_2$ HPP at 1.05 $cm^3\ g^{-1}$ and OVS-TBN-THS at 0.3 $cm^3\ g^{-1}$. The morphological characteristics of OVS-TBN-DBTH, OVS-TBN-THS, and OVS-TBN-THSO$_2$ HPPs were investigated using HR-TEM and FE-SEM. HR-TEM images revealed the presence of partially ordered porosity, indicating an organized arrangement of organic linkers, as illustrated in **Figure S10**.

Fig. 5 clearly illustrates, based on the FE-SEM images, that OVS-TBN-DBTH, OVS-TBN-THS, and OVS-TBN-THSO$_2$ HPPs consist of aggregated spherical particles with comparable irregular shapes, exhibiting a dense aggregation pattern.

Furthermore, the elemental mapping depicted in Fig. 6 indicates a uniform distribution of elements such as silicon (Si), carbon (C), oxygen (O), and sulfur (S) across the entire region of interest in all HPP materials. The atomic compositions of carbon (C), oxygen (O), silicon (Si), and sulfur (S) in the OVS-TBN-DBTH HPP [**Table S3**] were 48.82 %, 11.79 %, 34.36 %, and 5.03 %, respectively. In the case of the OVS-TBN-THS HPP, these compositions were 30.71 % for C, 22.73 % for O, 40.18 % for Si, and 6.38 % for S. Finally, in the OVS-TBN-THSO$_2$ HPP, the atomic compositions were 47.62 % for C, 11.72 % for O, 32.21 % for Si, and 8.45 % for S.

3.2. The adsorption of Rhodamine B dye using OVS-TBN-DBTH, OVS-TBN-THS, and OVS-TBN-THSO$_2$ HPPs as adsorbents

According to existing literature, Rhodamine B (RhB) can exist in three protonated forms with different charges: the zwitterion ($RhB^{\pm}$), RhBH+, and $RhBH^{22+}$. These forms predominate under specific pH conditions, with $RhB^{\pm}$ being more prevalent at pH levels above 4, $RhBH^{+}$ dominating in the pH range of 1–3, and $RhBH^{22+}$ being more common at pH values below 1. Additionally, RhB molecules have the capacity to combine and form larger molecular structures called dimers, and the extent of dimerization varies depending on the type of RhB species present; $RhB^{\pm}$ has a higher tendency to dimerize compared to the

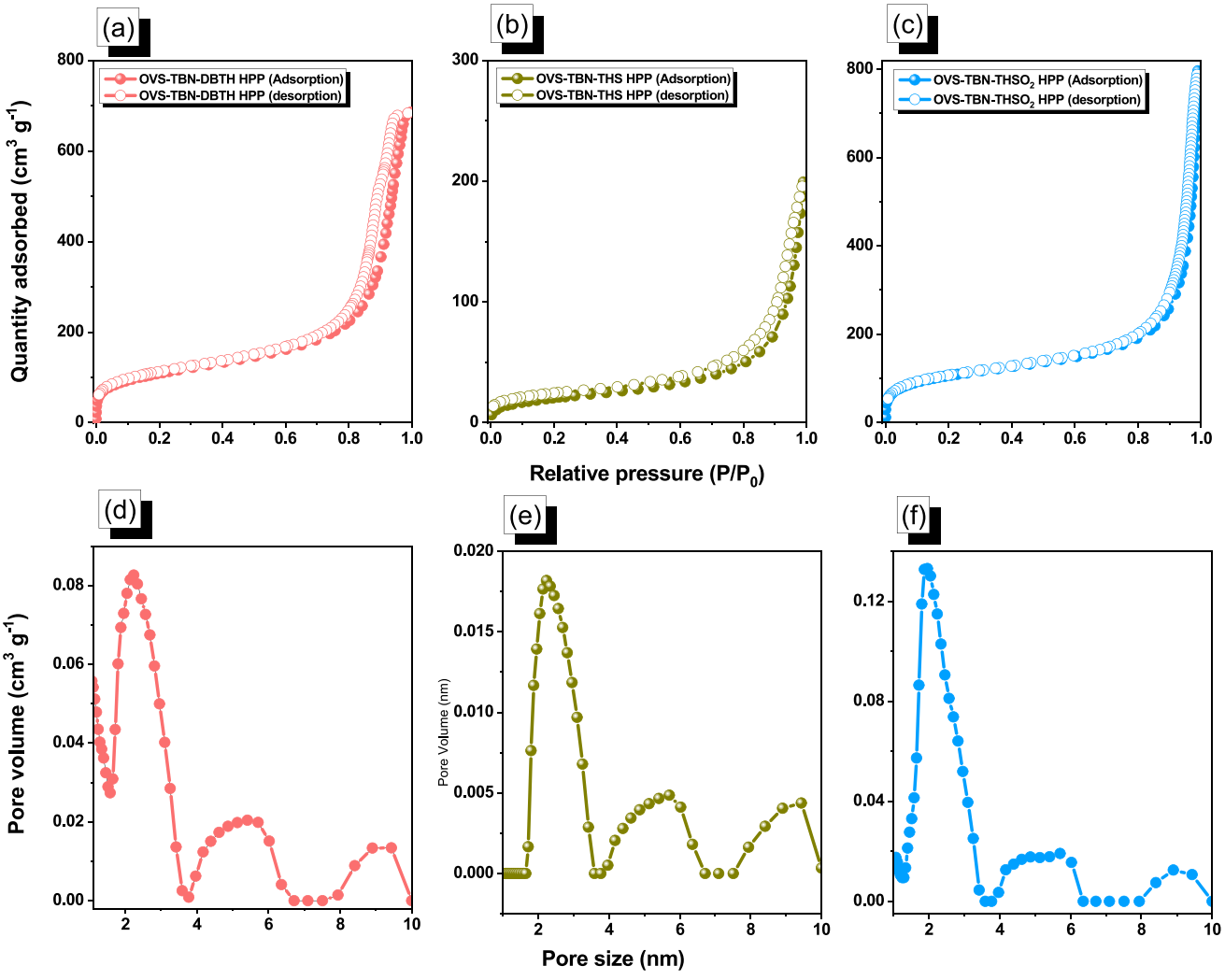

Fig. 4. (a-c) BET and (d-f) pore size analyses of OVS-TBN-DBTH (a, d), OVS-TBN-THS (b, e), and OVS-TBN-THSO$_2$ HPPs (c, f).

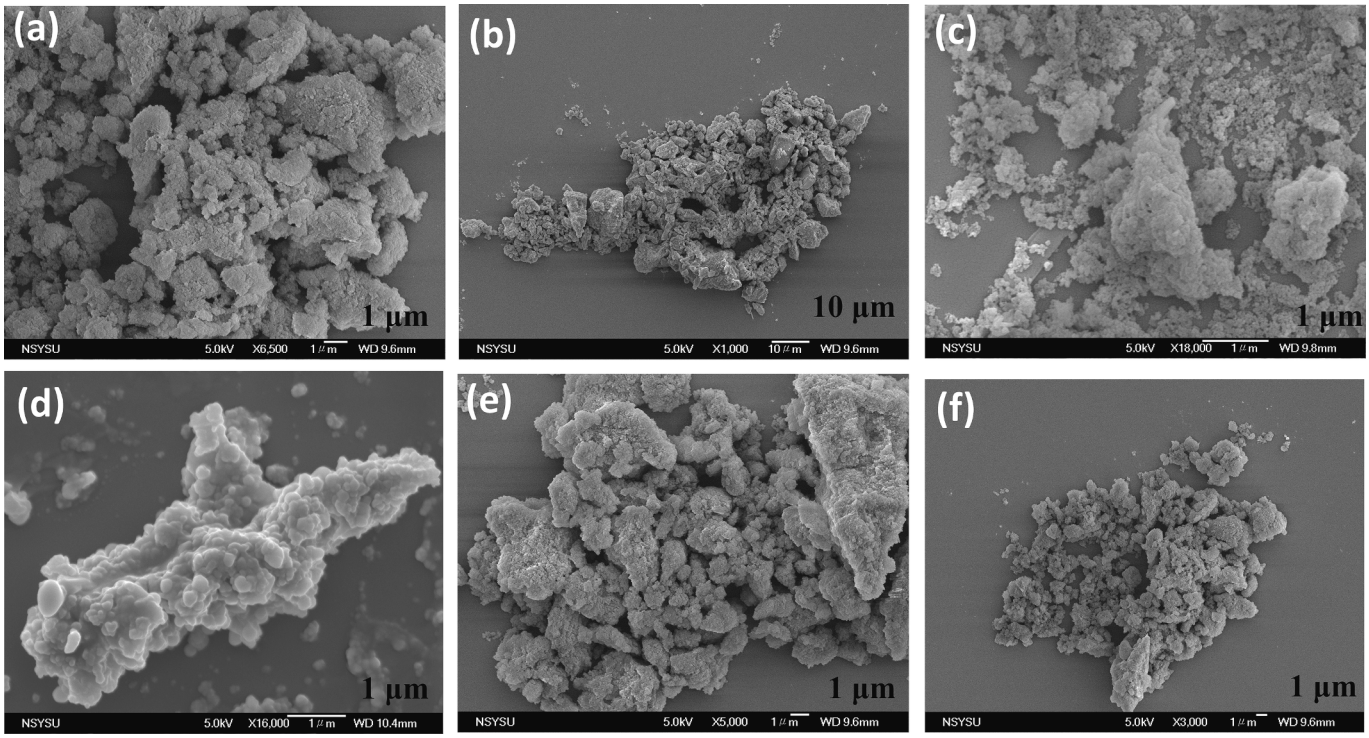

Fig. 5. SEM analyses of OVS-TBN-DBTH (a, B), OVS-TBN-THS (c, d), and OVS-TBN-THSO$_2$ HPPs (e, f).

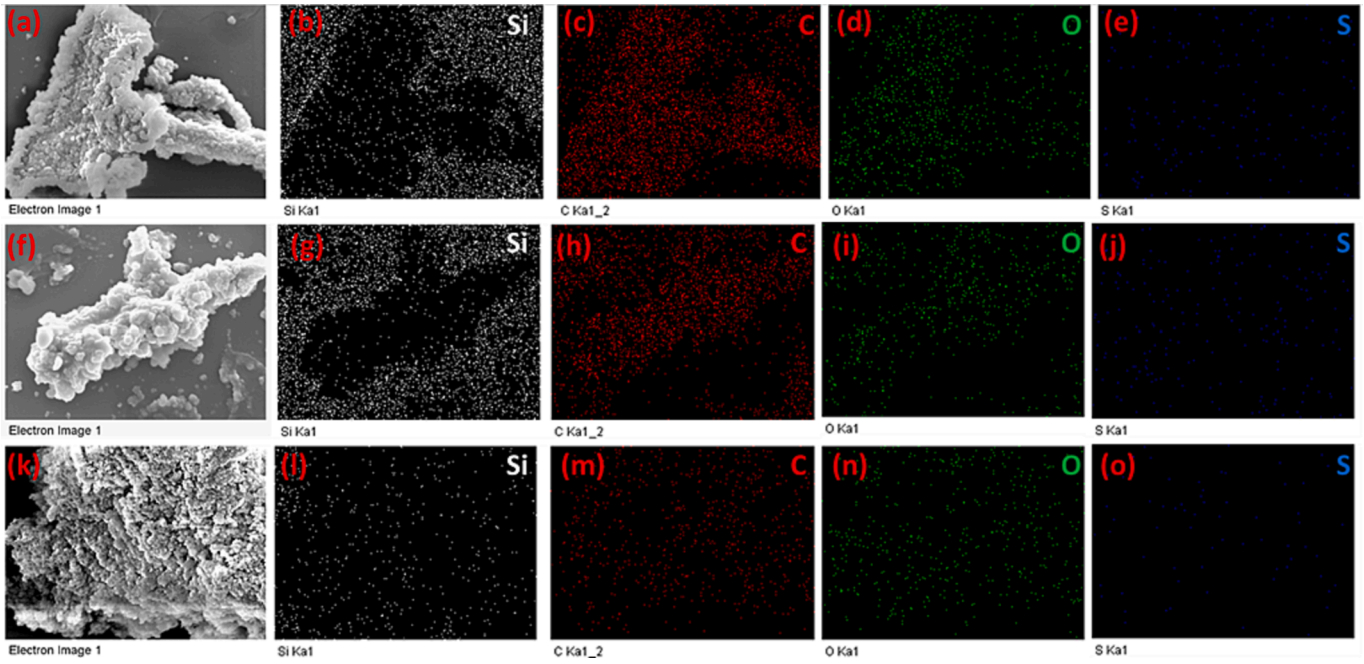

Fig. 6. SEM-EDS analyses (silicon (Si), carbon (C), oxygen (O), and sulfur (S) atoms) of OVS-TBN-DBTH (a-e), OVS-TBN-THS (f-j), and OVS-TBN-THSO$_2$ HPPs (k-o). The scale bar is 4 μm in all SEM images.

positively charged cations. One critical factor influencing the adsorption behavior is the pH of the solution. The study investigated how the pH affects dye removal, conducting experiments across a range of pH conditions (2)–(7), as illustrated in Fig. 7**(a-c)**. The results clearly indicate that the effectiveness of the synthesized OVS-TBN-DBTH, OVS-TBN-THS, and OVS-TBN-THSO$_2$ HPPs in dye removal is strongly influenced by the pH of the solution. Initially, the dye removal rate is relatively low, but it gradually increases as the solution pH rises, reaching its peak at around pH 4. Subsequently, the dye removal rate experiences a significant decrease as the pH continues to rise. This observed trend is likely due to the pH-induced formation of different ionic species and alterations in the surface charge of the carbon material. When the pH is below 4, RhB ions exist in a positively charged state, and they remain as monomeric molecules, facilitating their easy penetration into the pore structure of the adsorbent material. In contrast, at pH values above 4, RhB undergoes a transformation into a zwitterionic form in the aqueous

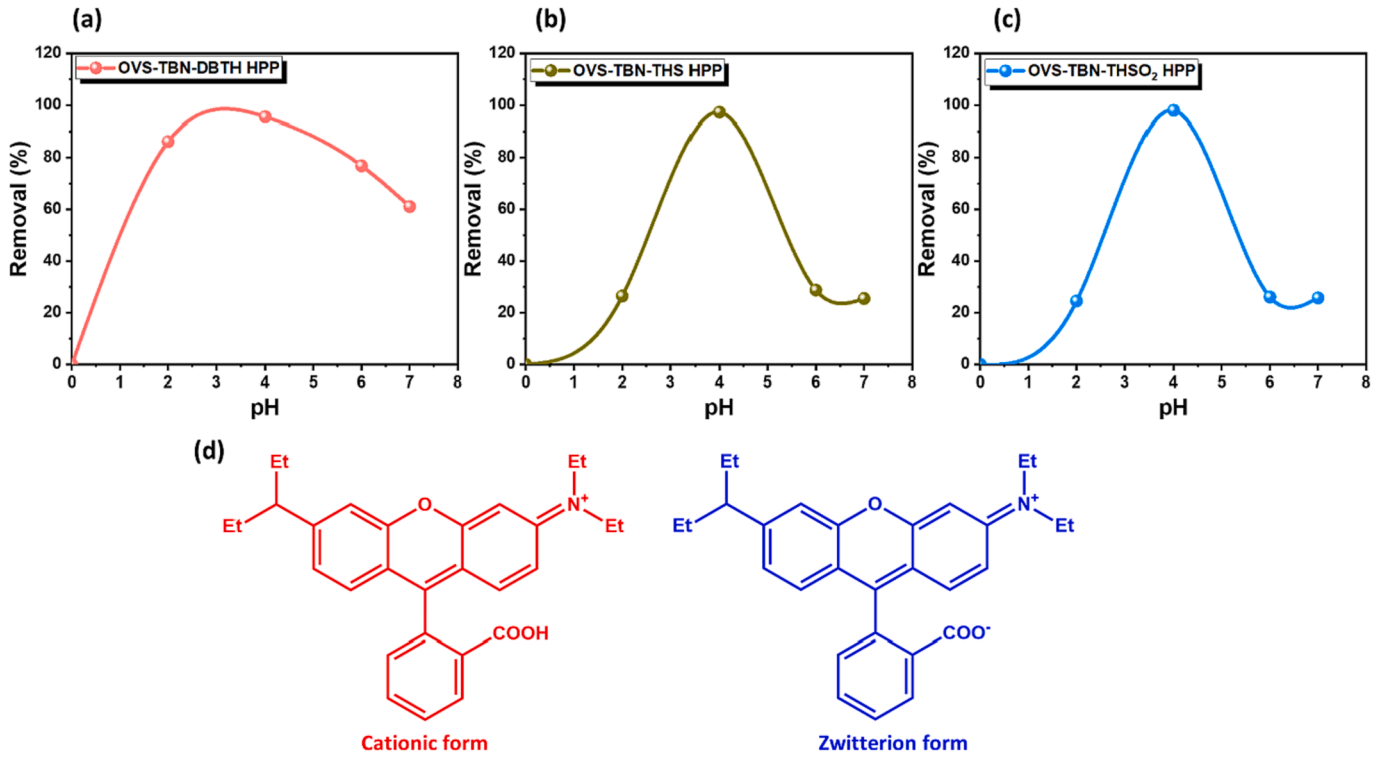

Fig. 7. Effect of initial pH solution on the adsorption of RhB onto (a) OVS-TBN-DBTH, (b) OVS-TBN-THS, and (c) OVS-TBN-$THSO_2$ HPPs. (d) Molecular form of RhB (cationic and zwitterionic form).

solution [Fig. 7**(d)**]. This transformation promotes the aggregation of RhB molecules, leading to the formation of larger molecular structures known as dimers [68]. Consequently, these aggregated zwitterionic forms face difficulty in accessing the pore structure due to their increased size. The enhanced aggregation of the zwitterionic form is primarily driven by attractive electrostatic interactions occurring between the carboxyl and xanthene groups of the individual monomers [22]. Interestingly, OVS-TBN-DBTH displayed notably high efficiency in dye removal (86 %) even at low pH conditions (pH 2), surpassing the performance of OVS-TBN-THS and OVS-TBN-$THSO_2$ HPPs (26.5 % and 24.5 %, respectively), as illustrated in Fig. 7. The low performance can be attributed to the protonation of the heteroatoms (S and O) in the polymers at low pH, resulting in repulsive forces between the positively charged heteroatoms and the cationic RhB.

3.3. Effect of contact time on the adsorption of Rhodamine B dye using OVS-based HPPs

Optimization of contact time is essential for the adsorption studies, to ensure complete equilibrium between the dye-adsorbent system. The effect of contact time on Rhodamine B dye removal is given in **Figure S11**. The effectiveness of the adsorption process using the synthesized materials was evaluated by examining the removal of RhB at various contact times, as depicted in Fig. 8**(a) and 8(b)**. Prior to the

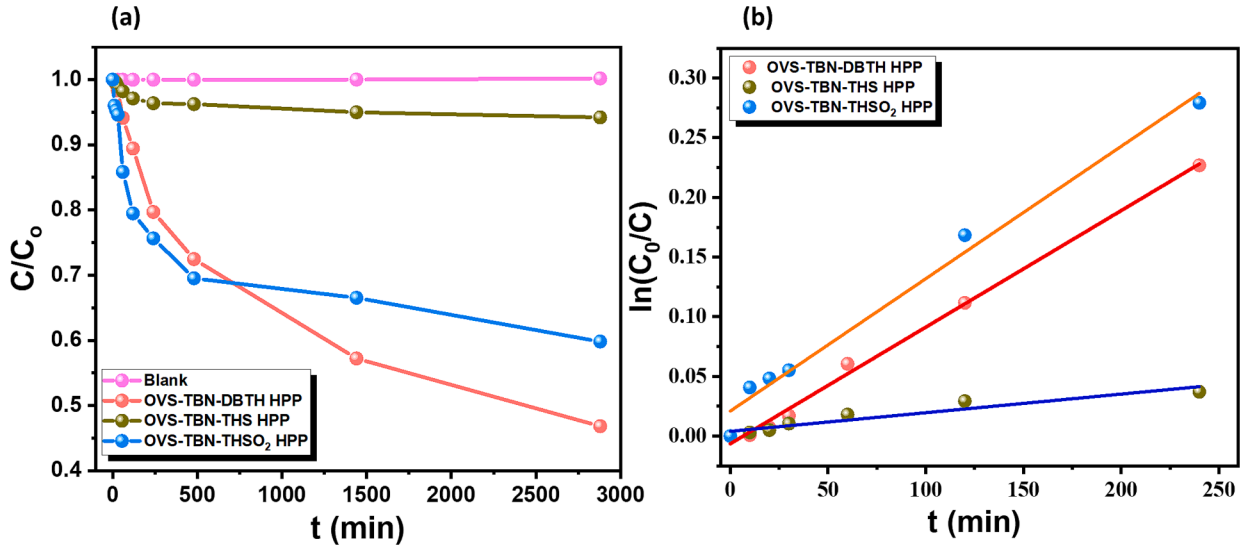

Fig. 8. (a) Adsorption of RhB with OVS-TBN-DBTH, OVS-TBN-THS, and OVS-TBN-$THSO_2$ HPPs; (b) kinetic data for the adsorption of RhB with three adsorbents.

adsorption experiments, a blank sample was conducted to establish the contribution of the as-synthesized materials to the adsorption process. As illustrated in Fig. 8**(b)**, the influence of contact time on the adsorption efficiency of RhB on three distinct adsorbents, namely OVS-TBN-DBTH, OVS-TBN-THS, and OVS-TBN-THSO$_2$ HPPs. The results indicate that the removal of RhB dye from these adsorbents proceeded rapidly during the initial phase, followed by a more gradual decline in dye removal until equilibrium was achieved, as shown in Fig. 8**(b) and S11**. This behavior can be attributed to the abundance of available adsorption sites during the initial phase, which gradually becomes depleted over time.

3.4. Kinetic studies of removal Rhodamine B dye using OVS-TBN-DBTH, OVS-TBN-THS, and OVS-TBN-THSO$_2$ HPPs as adsorbents

Kinetic models are often used to uncover the mechanisms behind the removal of substances from aqueous solutions and facilitate process engineering. Various mathematical models can be employed to analyze the kinetic data of adsorption, with the Lagergren rate equation being the most frequently used. In this study, the pseudo-first-order rate equation was utilized to examine the kinetics of the adsorption process, as presented below:

$$\frac{dq_1}{dt} = k_1(q_e - q_t) \tag{1}$$

In this equation, q_e and q_t represent the concentrations of the dye (in mg/g) at equilibrium and at the given time during the adsorption process, respectively. The parameter k_1 corresponds to the equilibrium rate constant associated with pseudo-first-order adsorption for the dye. On integration with limits from t = 0 to t and q = 0 to q_t, we have

$$\ln(q_e - q_t) = lnq_e - k_1 t \tag{2}$$

The adsorption rate constant (k_1) for rhodamine B adsorption on the three adsorbents was obtained by plotting ln (q_e-q_t) against time (t), as shown in Fig. 9**(a-c)**, and the resulting values are presented in Table 1.

Table 1
Kinetic parameters for adsorption of rhodamine B onto OVS-HPPs.

Adsorbent	Pseudo-first-order			Pseudo-second-order		
	q_{e1} (mg/g)	k_1 (min^{-1})	R^2	q_{e2} (mg/g)	k_2 (g mg^{-1} min^{-1})	R^2
OVS-TBN-DBTH HPP	30.24	0.00114	0.975	44.64	0.00002	0.815
OVS-TBN-THS HPP	16.11	0.00012	0.663	3.63	0.00143	0.995
OVS-TBN-THSO$_2$ HPP	15.28	0.00093	0.607	21.65	0.00023	0.980

However, the experimental data demonstrated considerable non-linearity, as evidenced by low correlation values and low qe values.

The kinetic data were evaluated using the pseudo-second-order kinetic model proposed by Ho and McKay. The corresponding differential equation is represented as:

$$\frac{dq_t}{dt} = k_2(q_e - q_t)^2 \tag{3}$$

The rate constant for pseudo-second-order adsorption equilibrium, represented as k_2 (in g/(mg min)), is defined. To transition from t = 0 to t = q_t, the integration of Equation (4) is required.

$$\frac{1}{q_e - q_t} = \frac{1}{q_e} + k_2 t \tag{4}$$

which is the integrated rate law for a pseudo-second-order reaction. Eq. (5) can be rearranged to obtain a linear form:

$$\frac{t}{q_t} = \frac{1}{k_2 q_e^2} + \left(\frac{1}{q_e}\right)t \tag{5}$$

To determine the rate parameters, t/q_t was plotted against time and the resulting linear plots were used, as shown in Fig. 9**(d-f)**. From these

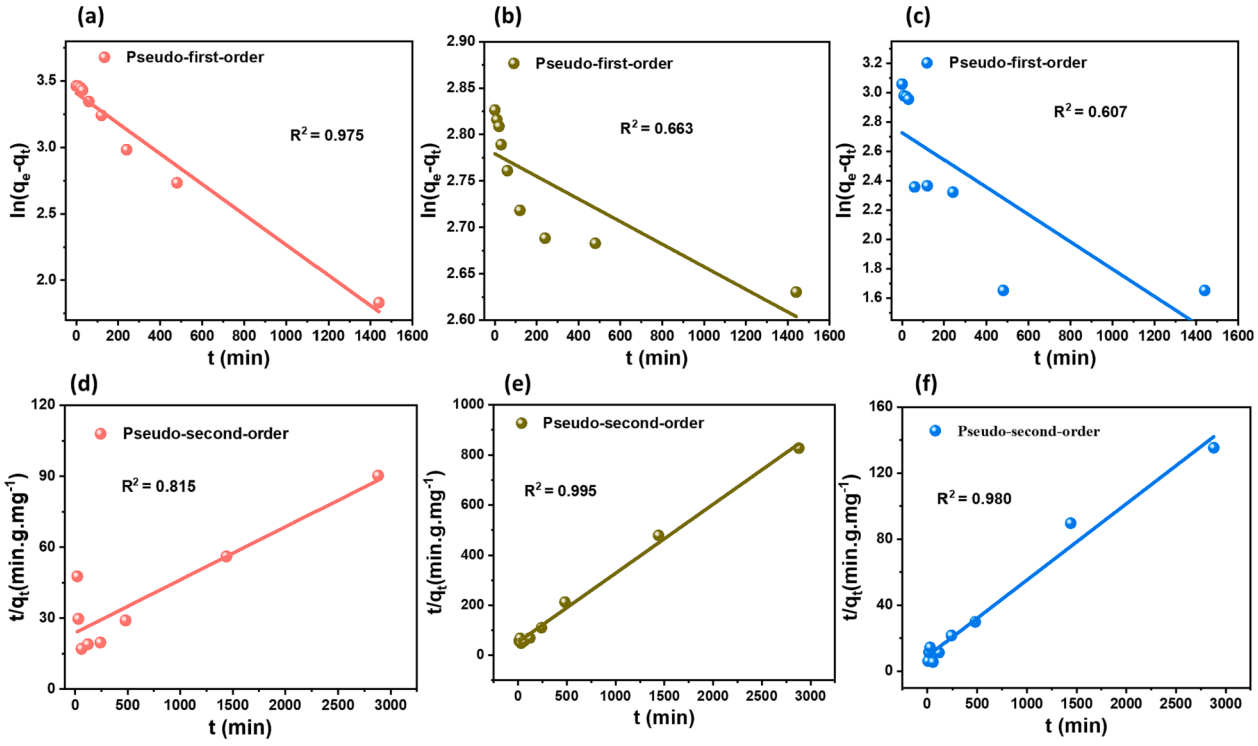

Fig. 9. (a)-(c) Pseudo-first-order kinetic fitting of OVS-TBN-DBTH, OVS-TBN-THS, and OVS-TBN-THSO$_2$ HPPs, respectively and (d)-(f) Pseudo-second-order kinetic fitting of OVS-TBN-DBTH, OVS-TBN-THS, and OVS-TBN-THSO$_2$ HPPs, respectively.

plots, the values of k_2, q_e, and correlation coefficients (R_2^2) for the dye solution were calculated and are presented in Table 1.

In the case of RB adsorption onto OVS-TBN-DBTH HPP, the pseudo-first-order model provided the best fit to the data, indicating that the adsorption process is primarily driven by physisorption. As the number of sulfur atoms increased, the pseudo-second-order model proved to be a better representation of the adsorption system for rhodamine B by OVS-TBN-THS, and OVS-TBN-THSO$_2$ HPP. In contrast to pseudo-first-order kinetics, it was observed that the correlation coefficients for pseudo-second-order kinetics were closer to unity.

3.5. Diffusion study of RhB dye onto OVS-HPPs

The adsorption process of an adsorbate from an aqueous solution onto an adsorbent encompasses several sequential steps, including bulk diffusion, film diffusion, pore diffusion, and binding to active sites on the adsorbent. The rate of this process is determined by the slowest step, which can either be film diffusion or intraparticle diffusion. To discern the underlying diffusion mechanism, kinetic data for the adsorption of RhB dye onto OVS-TBN-DBTH, OVS-TBN-THS, and OVS-TBN-THSO$_2$ HPPs were evaluated using the intraparticle (**Eq. (6)** diffusion model proposed by Weber and Morris, as expressed by the respective equations.

$$q_t = K_i t^{0.5} + C \quad (6)$$

The intraparticle diffusion rate constant (K_i) and the intercept (C), related to the boundary layer thickness, are integral parameters in these models. According to the Weber and Morris model, intraparticle diffusion is considered the rate-controlling step if the plot of q_t (amount of adsorbate adsorbed) against $t^{1/2}$ (square root of time) forms a linear relationship passing through the origin.

The analysis of time-dependent data for RhB dye adsorption onto OVS-TBN-DBTH, OVS-TBN-THS, and OVS-TBN-THSO$_2$ HPPs was presented in Fig. 10**(a-c)**. Fig. 10 displayed a multilinear pattern in the plot of qt versus $t^{1/2}$, indicating distinct stages of the adsorption process. The initial linear stage was attributed to external surface adsorption, denoting film diffusion, while the subsequent stage suggested intraparticle diffusion. The third stage corresponded to the equilibrium, where intraparticle diffusion began to decelerate due to the exceedingly low concentration of RhB dye remaining in the solution with a decrease in interior active sites. The calculation of K_i and C values was carried out from the slope and intercept of the second linear stage, and the results were documented in Table 2. However, the plot of qt versus $t^{1/2}$ from Fig. 10 did not exhibit a linear relationship passing through the origin,

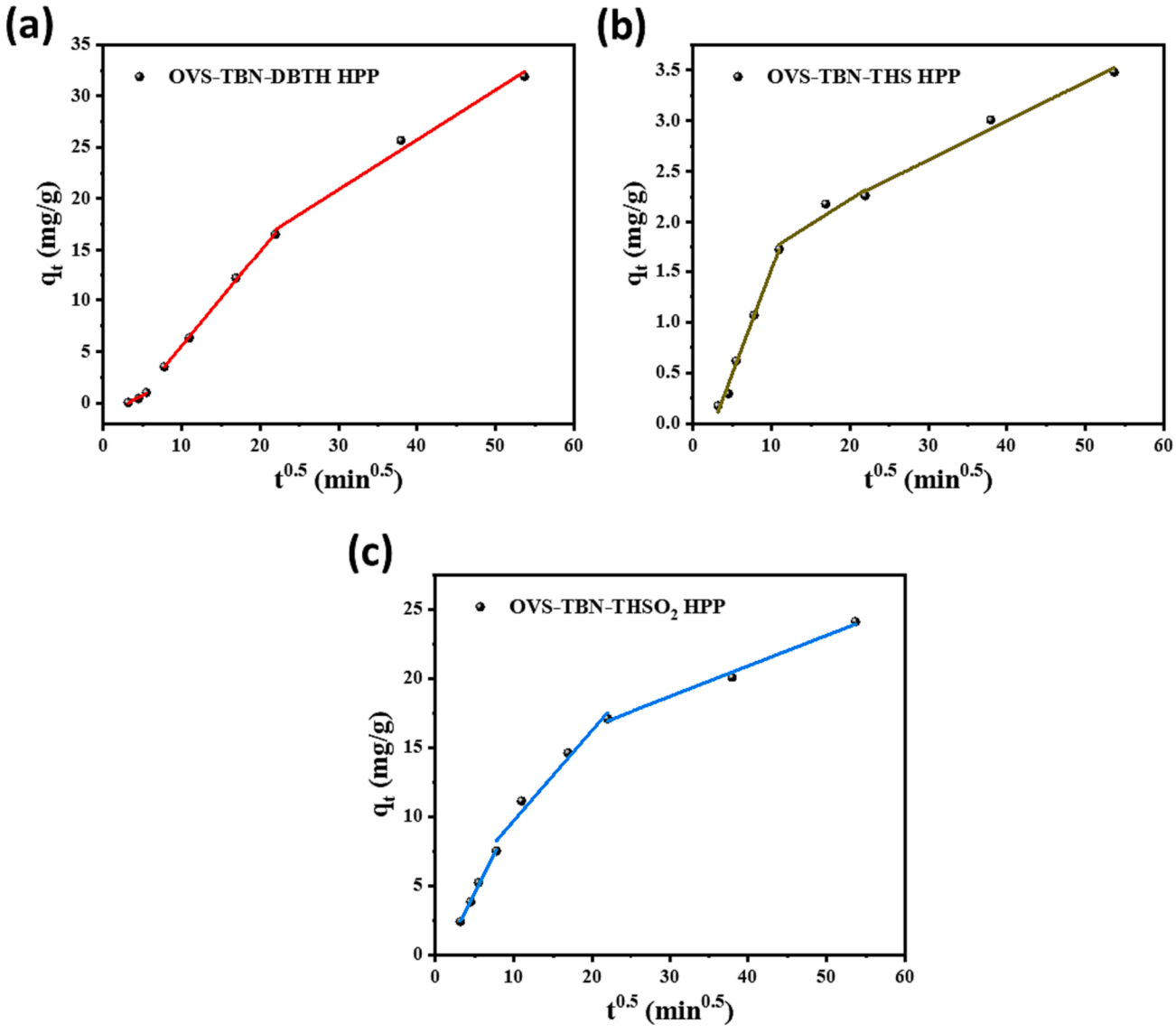

Fig. 10. Intraparticle diffusion of RhB dye onto (a) OVS-TBN-DBTH, (b) OVS-TBN-THS, and (c) OVS-TBN-THSO$_2$ HPPs.

Table 2
Intraparticle diffusion parameters of RhB dye onto OVS-HPPs.

Adsorbent	K_i	C	R^2
OVS-TBN-DBTH HPP	0.927	3.692	0.999
OVS-TBN-THS HPP	0.049	1.242	0.946
OVS-TBN-$THSO_2$ HPP	0.655	3.167	0.986

which is a requirement for the Weber and Morris model, signifying the inapplicability of this model. Consequently, intraparticle diffusion was not identified as the rate-controlling step during the adsorption of RhB dye onto OVS-TBN-DBTH, OVS-TBN-THS, and OVS-TBN-$THSO_2$ HPPs.

3.6. Adsorption isotherm studies of removal of Rhodamine B dye using OVS-TBN-DBTH, OVS-TBN-THS, and OVS-TBN-$THSO_2$ HPPs as adsorbents

Adsorption isotherms play an important role in explaining the way adsorbents react with an adsorbent. It is very important in showing the effectiveness of the use of adsorbents. Thus, it is necessary to examine the results obtained from studies on isotherms, as this evaluation allows us to determine the degree of attraction between an adsorbate and a given adsorbent. The adsorption experiments were conducted in batch mode. A series of Rhodamine B dye solutions with varying concentrations were prepared (10–150 mg/L). A predetermined amount of each HPP was added to the dye solution, and the mixture was agitated at a constant temperature until equilibrium was reached. The equilibrium concentrations of Rhodamine B dye in the solution were determined spectrophotometrically.

The concentration-dependent adsorption study of Rhodamine B onto OVS-TBN-DBTH, OVS-TBN-THS, and OVS-TBN-$THSO_2$ HHPs demonstrates the relationship between equilibrium adsorbate concentration (C_e) and adsorption capacity (q_e) as shown in Fig. 11**(a-c)**. The results show that increasing the adsorbate concentration enhances the adsorption capacity of HPPs, reaching a plateau at higher C_e values. This increase in adsorption capacity can be attributed to the higher mass driving force at elevated adsorbate concentrations, allowing more RhB molecules to be adsorbed onto the HPPs' surfaces. The maximum adsorption capacities of 65.78 mg/g, 42.12 mg/g, and 62.48 mg/g were obtained for OVS-TBN-DBTH, OVS-TBN-THS, and OVS-TBN-$THSO_2$ HPPs, respectively (Fig. 11), indicating their potential as efficient adsorbents for Rhodamine B removal from aqueous solutions.

The Langmuir isotherm model and the Freundlich isotherm model [Fig. 12**(a-f)**] were employed to match the observed RhB adsorption data. These isotherm models are the most comprehensive and straightforward equations used to describe the adsorption phenomenon. Equations (7) and (8) represent the linear representations of the Langmuir and Freundlich models, respectively, and the associated parameters can be found in Table 3.

$$\frac{C_e}{q_e} = \frac{1}{q_{max} \times K_L} + \frac{C_e}{q_{max}} \tag{7}$$

$$log q_e = \log K_F + \frac{1}{n} \log C_e \tag{8}$$

Where C_e represents the concentration of RhB in the liquid phase (mg/

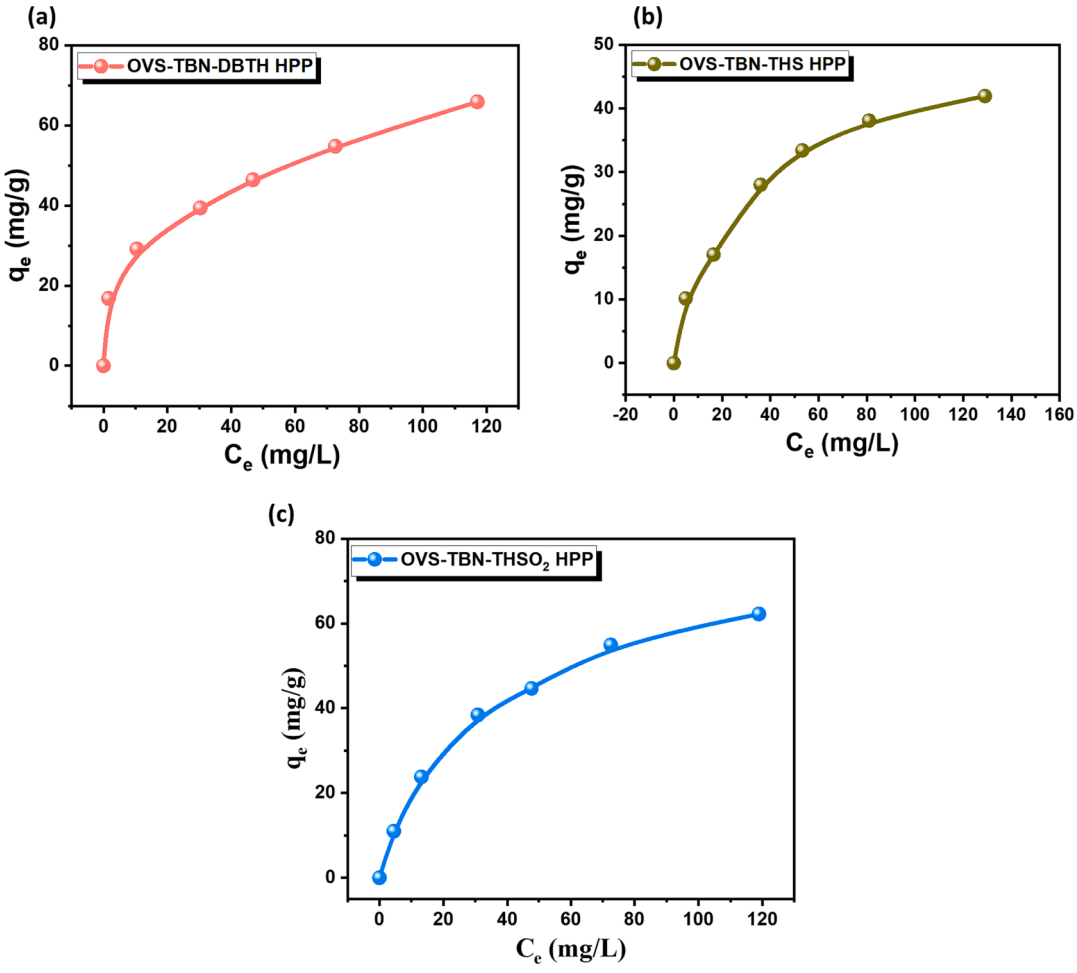

Fig. 11. Adsorption isotherm of RhB dye onto (a) OVS-TBN-DBTH, (b) OVS-TBN-THS, and (c) OVS-TBN-$THSO_2$ HPPs.

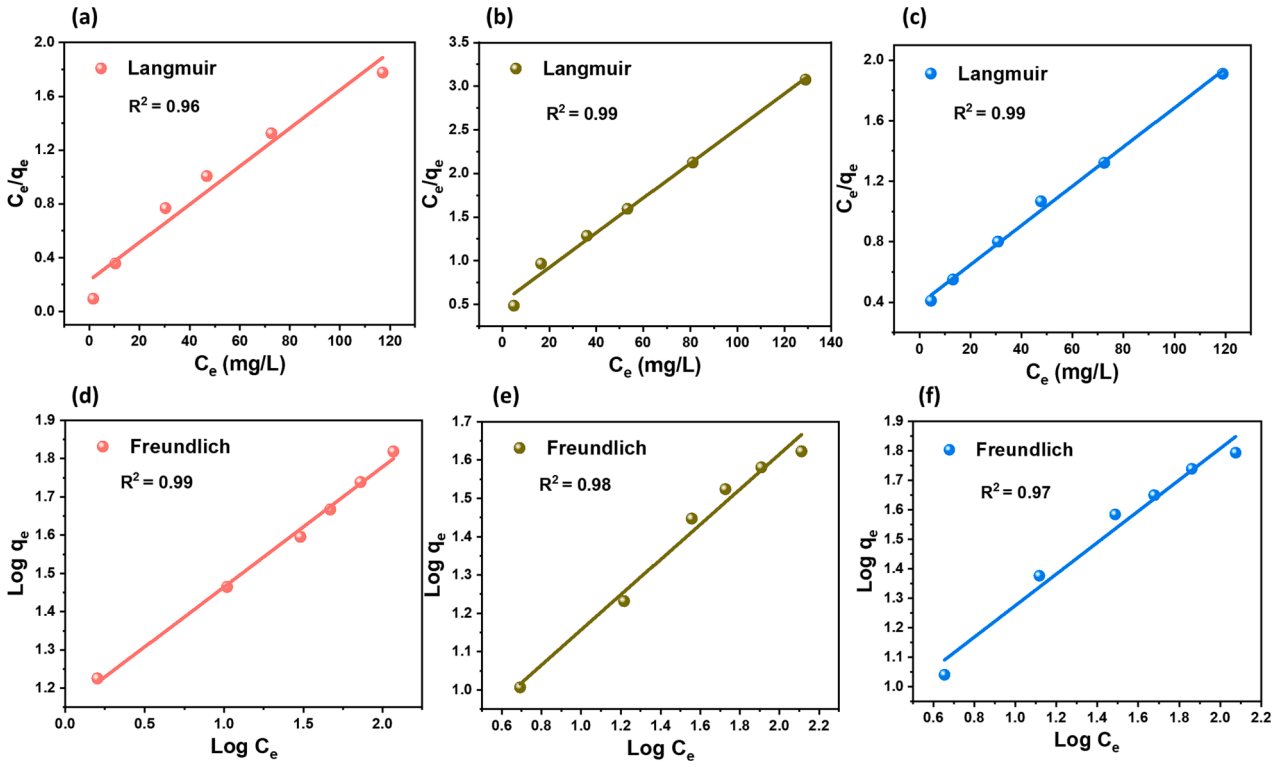

Fig. 12. (a)-(c) Langmuir fitting of OVS-TBN-DBTH, OVS-TBN-THS, and OVS-TBN-$THSO_2$ HPPs, respectively and (d)-(f) Freundlich fitting of OVS-TBN-DBTH, OVS-TBN-THS, and OVS-TBN-$THSO_2$ HPPs, respectively.

Table 3
Isotherm parameters for adsorption of rhodamine B onto OVS-HPPs.

Adsorbent	Langmuir			Freundlich		
	q_{max} (mg/g)	K_L (L/mg)	R^2	K_F (mg^{1-n} L^n/g)	1/n	R^2
OVS-TBN-DBTH HPP	70.62	0.061	0.96	14.16	0.313	0.99
OVS-TBN-THS HPP	50.20	0.038	0.99	4.99	0.458	0.98
OVS-TBN-$THSO_2$ HPP	77.10	0.033	0.99	5.53	0.533	0.97

L). q_e refers to the equilibrium adsorption of RhB by OVS-HPPs (mg/g), while q_{max} represents the maximum adsorption capacity of OVS-HPPs (mg/g). The Langmuir (K_L, L/mg) and Freundlich (K_F, mg^{1-n} L^n/g) isotherm constants are related to the adsorption energy and the adsorption capacity, respectively.

The correlation coefficient (R^2) for the Freundlich isotherm model, with a value of 0.99, was significantly greater than that of the Langmuir isotherm (R^2, 0.96) for OVS-TBN-DBTH HPP, indicating that the adsorption of RhB by OVS-TBN-DBTH HPP occurs in multiple layers. Nevertheless, for OVS-TBN-THS and OVS-TBN-$THSO_2$ HPP, the correlation coefficient (R^2) of the Langmuir isotherm model, standing at 0.99, exceeded that of the Freundlich isotherm (R^2, 0.98 and 0.97, respectively). suggesting that the adsorption of RhB by OVS-TBN-THS, and OVS-TBN-$THSO_2$ HPP occurs in a monolayer (Fig. 12).

3.7. Adsorption of Rhodamine B onto OVS-TBN-DBTH, OVS-TBN-THS, and OVS-TBN-$THSO_2$ HPPs as adsorbents: Temperature dependence and thermodynamic parameters

The adsorption of Rhodamine B onto OVS-TBN-DBTH, OVS-TBN-THS, and OVS-TBN-$THSO_2$ HPPs has been investigated across a range of temperatures, specifically within the range of 30 to 70 °C. This temperature variation was examined due to the potential influence of Brownian motion on the adsorption process. Upon subjecting the system to differing temperatures, a remarkable trend emerged. The adsorption of Rhodamine B onto the three distinct OVS-HPPs exhibited a significant increase as the temperature was elevated from 30 to 70 °C. This observation underscores the temperature-dependent nature of the adsorption process, suggesting that temperature plays a direct role in shaping the adsorption behavior of Rhodamine B on OVS-HPPs.

To gain deeper insights into the thermodynamics of this adsorption process, various thermodynamic parameters were computed using Equations (9), (10), and (11). These key parameters include the enthalpy change (ΔH°), entropy change (ΔS°), and free energy (ΔG°). These thermodynamic analyses provide essential information for understanding the energetics and spontaneity of the adsorption of Rhodamine B onto OVS-HPPs, shedding light on the underlying mechanisms governing this interaction.

$$\ln K_d = \frac{\Delta S^o}{R} - \frac{\Delta H^o}{RT} \tag{9}$$

$$K_d = \left(\frac{C_i - C_f}{A_f}\right) \times \frac{V}{M} \tag{10}$$

$$\Delta G^o = -RTlnK_d \tag{11}$$

where C_i and C_f, which denote the initial and final concentrations of the Rhodamine B solution, respectively; V, representing the volume of the solution (in mL); M, signifying the weight of OVS-HPPs (in grams); R, denoting the ideal gas constant (where R = 0.008314 kJ/mol); and T, representing the absolute temperature (in Kelvin).

The linear plot of $\ln K_d$ against 1/T, as depicted in Fig. 13, served as a valuable tool for determining the thermodynamic parameters of interest. Specifically, the slope and intercept of this plot were employed to calculate the values of the enthalpy change (ΔH°) and entropy change (ΔS°), respectively. Table 4 provides a concise summary of the

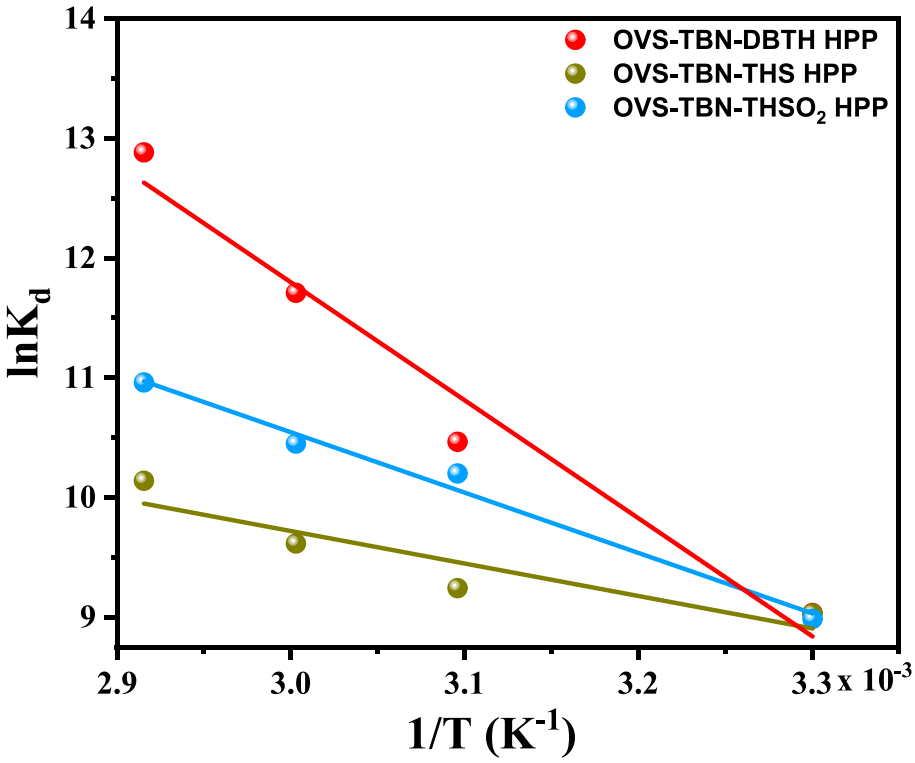

Fig. 13. Plot of $\ln K_d$ versus 1/T for adsorption of Rhodamine B onto OVS-HPPs.

Table 4
Thermodynamic parameters for adsorption of Rhodamine B onto OVS-HPPs.

Polymer	ΔG° (kJ/mol)				ΔH°	ΔS°	R^2
	303 K	323 K	333 K	343 K	(kJ/mol)	(kJ/mol K^{-1})	
OVS-TBN-DBTH	−22.762	−28.087	−32.419	−34.463	81.871	0.344	0.969
OVS-TBN-THS	−22.748	−24.822	−26.622	−28.915	22.539	0.148	0.848
OVS-TBN-$THSO_2$	−22.637	−27.392	−28.931	−31.255	41.885	0.213	0.987

computed thermodynamic values pertaining to the adsorption of Rhodamine B onto OVS-HPPs. Notably, the negative values of ΔG° at various temperatures suggest that the adsorption process is both feasible and spontaneous. The observation that ΔH° is positive indicates that the adsorption is an endothermic process. Furthermore, the positive value of ΔS° implies that there is an element of randomness or increased entropy during the adsorption of Rhodamine B onto OVS-HPPs [69]. This indicates that the system becomes more disordered as the adsorption takes place, shedding light on the nature of the adsorption process from a thermodynamic perspective. As depicted in **Figure S12**, the results from the recyclability assessments of the most promising sample, OVS-TBN-DBTH HPP, demonstrate that even after six experimental cycles, the RhB removal rate by OVS-TBN-DBTH HPP consistently remained at a high level.

Table S4 presents an analysis of the dye adsorption abilities of OVS-TBN-DBTH, OVS-TBN-THS, and OVS-TBN-$THSO_2$ HHPs compared to other materials.

4. Conclusions

To summarize, three distinct OVS materials, namely OVS-TBN-DBTH, OVS-TBN-THS, and OVS-TBN-$THSO_2$ HPPs, were synthesized using the Heck reaction. Among these materials, OVS-TBN-DBTH HPP exhibits superior characteristics in terms of surface area (387 m^2/g), pore size (2.3 nm), and thermal stability with a T_{d10} of 57 5 °C. Following 48 h of adsorption experiments using rhodamine B, OVS-TBN-DBTH HPP displays the lowest concentration of rhodamine B in solution, indicating its stronger adsorption capability compared to the other two samples. Under optimal conditions (utilizing 5 mg of each HPP material and subjecting them to 25 mg/L of rhodamine B at 25 °C), the maximum adsorption capacities were determined to be 65.78 mg/g, 42.12 mg/g, and 62.48 mg/g for OVS-TBN-DBTH, OVS-TBN-THS, and OVS-TBN-$THSO_2$ HPPs, respectively. The kinetic studies for the OVS-TBN-DBTH HPP adsorption system are best described by the pseudo-first-order model, indicating that physisorption predominantly governs the adsorption process. On the other hand, the pseudo-second-order model provides the best fit for OVS-TBN-THS, and OVS-TBN-$THSO_2$ HPPs, mainly due to the increased presence of S atoms in these materials.

This effective synthetic technique, combined with the advantageous surface area derived from the unique structural features of these building blocks [OVS nanoparticles, TBN, DBTH, THS and $THSO_2$], underscores the significant potential of these HPPs for water treatment applications.

CRediT authorship contribution statement

Ching-Wen Hsiao: Investigation. **Ahmed M. Elewa:** Investigation, Methodology, Writing – original draft. **Mohamed Gamal Mohamed:** Investigation, Methodology, Conceptualization, Supervision, Writing – original draft. **Shiao-Wei Kuo:** Supervision.

Declaration of Competing Interest

The authors declare that they have no known competing financial interests or personal relationships that could have appeared to influence the work reported in this paper.

Data availability

The data that has been used is confidential.

Acknowledgments

This study was supported financially by the Ministry of Science and Technology, Taiwan, under contracts NSTC 110-2124-M-002-013 and 111-2223-E-110-004. The authors thank the staff at National Sun Yat-sen University for their assistance with the TEM (ID: EM022600) experiments.

Appendix A. Supplementary data

Supplementary data to this article can be found online at https://doi.org/10.1016/j.seppur.2023.125771.

References

[1] I. Ali, New generation adsorbents for water treatment, Chemical Reviews 122 (2012) 5073–5091, https://doi.org/10.1021/cr300133d.
[2] H. Sadegh, G.A.M. Ali, V.K. Gupta, A.S.H. Makhlouf, R. Shahryari-ghoshekandi, M. N. Nadagouda, M. Sillanpää, E. Megiel, The role of nanomaterials as effective adsorbents and their applications in wastewater treatment, J. Nanostruct. Chem. 7 (2017) 1–14, https://doi.org/10.1007/s40097-017-0219-4.
[3] M. Afshari, M. Dinari, Synthesis of new imine-linked covalent organic framework as high efficient absorbent and monitoring the removal of direct fast scarlet 4BS textile dye based on mobile phone colorimetric platform, Journal of Hazardous Materials 385 (2020), 121514, https://doi.org/10.1016/j.jhazmat.2019.121514.
[4] R. Bera, M. Ansari, S. Mondal, N. Das, Selective CO_2 capture and versatile dye adsorption using a microporous polymer with triptycene and 1,2,3-triazole motifs, European Polymer Journal 99 (2018) 259–267, https://doi.org/10.1016/j.eurpolymj.2017.12.029.
[5] J. Tang, R. Xu, G. Sui, D. Guo, Z. Zhao, S. Fu, X. Yang, Y. Li, J. Li, Double-shelled porous g-C_3N_4 nanotubes modified with amorphous cu-doped FeOOH nanoclusters as 0D/3D non-homogeneous photo-fenton catalysts for effective removal of organic dyes, Small 19 (2023) 202208232, https://doi.org/10.1002/smll.202208232.
[6] W. Gong, Q. Wu, L. Ma, W. Zhang, X. Li, A. Xu, S. Zhao, MnO_x/g-C_3N_4 nanocomposites mediated sulfite activation for enhanced organic pollutants degradation under visible light irradiation, Colloids and Surfaces. A, Physicochemical and Engineering Aspects 659 (2022), 130598, https://doi.org/10.1016/j.colsurfa.2022.130812.
[7] R. Xu, J. Li, G. Sui, Y. Zhuang, D. Guo, Z. Luo, S. Liang, H. Yao, C. Wang, S. Chen, Constructing supramolecular self-assembled porous g-C_3N_4 nanosheets containing thiophene-groups for excellent photocatalytic performance under visible light, Applied Surface Science 578 (2022), 152064, https://doi.org/10.1016/j.apsusc.2021.152064.
[8] J. Núñez, M. Yeber, N. Cisternas, R. Thibaut, P. Medina, C. Carrasco, Application of electrocoagulation for the efficient pollutants removal to reuse the treated wastewater in the dyeing process of the textile industry, Journal of Hazardous Materials 371 (2019) 705–711, https://doi.org/10.1016/j.jhazmat.2019.03.030.
[9] D. Lan, H. Zhu, J. Zhang, S. Li, Q. Chen, C. Wang, T. Wu, M. Xu, Adsorptive removal of organic dyes via porous materials for wastewater treatment in recent decades: A review on species, mechanisms and perspectives, Chemosphere 293 (2022), 133464, https://doi.org/10.1016/j.chemosphere.2021.133464.
[10] S. Afroze, T.K. Sen, A review on heavy metal ions and dye adsorption from water by agricultural solid waste adsorbents, Water, Air, and Soil Pollution 229 (2018) 1–50, https://doi.org/10.1007/s11270-018-3869-z.
[11] A.A. Al-Gheethi, Q.M. Azhar, P. Senthil Kumar, A.A. Yusuf, A.K. Al-Buriahi, R.M. S. Radin Mohamed, M.M. Al-Shaibani, Sustainable approaches for removing Rhodamine B dye using agricultural waste adsorbents: a review, Chemosphere 287 (2022), 132080, https://doi.org/10.1016/j.chemosphere.2021.132080.
[12] D. Xu, H. Ma, Degradation of rhodamine B in water by ultrasound-assisted TiO_2 photocatalysis, Journal of Cleaner Production 313 (2021), 127758, https://doi.org/10.1016/j.jclepro.2021.127758.
[13] L. Jin, Y.L. Li, J. Zhou, C.M. Huang, X. Liu, Rhodamine B as an efficient multifunctional passivator for the improvement of perovskite solar cell performance, Journal of Materials Chemistry C 11 (2023) 9189–9200, https://doi.org/10.1039/D3TC00818E.
[14] M.A. Arasi, A. Salem, S. Salem, Extraction of nano-porous silica from hydrosodalite produced via modification of low-grade kaolin for removal of methylene blue from wastewater, Journal of Chemical Technology and Biotechnology 95 (2020) 1989–2000, https://doi.org/10.1002/jctb.6387.
[15] Z. Chai, B. Liu, P. Lv, Y. Bai, J. Wang, X. Song, W. Su, G. Yu, Recycling of coal gasification fine slag as ultra-high capacity adsorbents for the removal of Rhodamine B dye: Graded synthesis method, kinetics and adsorption mechanism, Fuel 333 (2023), 126318, https://doi.org/10.1016/j.fuel.2022.126318.
[16] U. Jinendra, D. Bilehal, B.M. Nagabhushana, A.P. Kumar, Adsorptive removal of Rhodamine B dye from aqueous solution by using graphene–based nickel nanocomposite, Heliyon 7 (2021) e06851.
[17] R.D. Saini, Textile organic dyes: polluting effects and elimination methods from textile waste water, Int. J. Chem. Eng. Res. 9 (2017) 121–136.
[18] B. Lellis, C.Z. Fávaro-Polonio, J.A. Pamphile, J.C. Polonio, Effects of textile dyes on health and the environment and bioremediation potential of living organisms, Biotechnol. Res. Innov. 3 (2019) 275–290, https://doi.org/10.1016/j.biori.2019.09.001.
[19] W.S. Koe, J.W. Lee, W.C. Chong, Y.L. Pang, L.C. Sim, An overview of photocatalytic degradation: photocatalysts, mechanisms, and development of photocatalytic membrane Environ, Sci. Pollut. Res. 27 (2020) 2522–2565, https://doi.org/10.1007/s11356-019-07193-5.
[20] T. Guo, X. Fan, X. Jiang, Y. Qi, Jianping Du, Aiming Zhang, Hongtao Wang. Engineering shape of BiOCl nanosheets with improved visible-light response for superior photocatalytic degradation of Rhodamine B, Journal of Alloys and Compounds 948 (2023), 169586, https://doi.org/10.1016/j.jallcom.2023.169586.
[21] P.P. Selvam, S. Preethi, P. Basakaralingam, N. Thinakaran, A. Sivasamy, S. Sivanesan, Removal of rhodamine B from aqueous solution by adsorption onto sodium montmorillonite, Journal of Hazardous Materials 155 (2008) 39–44, https://doi.org/10.1016/j.jhazmat.2007.11.025.
[22] H.M. Gad, A.A. El-Sayed, Activated carbon from agricultural by-products for the removal of Rhodamine-B from aqueous solution, Journal of Hazardous Materials 168 (2009) 1070–1081, https://doi.org/10.1016/j.jhazmat.2009.02.155.
[23] T.O. Ajiboye, O.A. Oyewo, D.C. Onwudiwe, Adsorption and photocatalytic removal of Rhodamine B from wastewater using carbon-based materials, FlatChem 29 (2021), 100277, https://doi.org/10.1016/j.flatc.2021.100277.
[24] L. Peng, P. Qin, M. Lei, Q. Zeng, H. Song, J. Yang, J. Shao, B. Liao, J. Gu, Modifying Fe_3O_4 nanoparticles with humic acid for removal of Rhodamine B in water, Journal of Hazardous Materials 209 (2012) 193–198, https://doi.org/10.1016/j.jhazmat.2012.01.011.
[25] X. Zhao, D. Wang, C. Xiang, F. Zhang, L. Liu, X. Zhou, H. Zhang, Facile synthesis of boron organic polymers for efficient removal and separation of methylene blue, rhodamine B, and rhodamine 6G, ACS Sustainable Chemistry & Engineering 6 (2018) 16777–16787, https://doi.org/10.1021/acssuschemeng.8b04049.
[26] X.-C. Du, J.-H. Zhu, Z.-J. Quan, X.-C. Wang, Adsorption of rhodamine B by organic porous materials rich in nitrogen, oxygen, and sulfur heteroatoms, New Journal of Chemistry 45 (2021) 3448–3453, https://doi.org/10.1039/D0NJ05750A.
[27] Y. Han, W. Li, J. Zhang, H. Meng, Y. Xu, X. Zhang, Adsorption behavior of Rhodamine B on nanoporous polymers, RSC Advances 5 (2015) 104915–104922, https://doi.org/10.1039/C5RA21130A.
[28] H. Wang, N. Qiu, X. Kong, Z. Hu, F. Zhong, Y. Li, H. Tan, Novel Carbazole-Based Porous Organic Polymer for Efficient Iodine Capture and Rhodamine B Adsorption, ACS Applied Materials & Interfaces 15 (2023) 14846–14853, https://doi.org/10.1021/acsami.3c00918.
[29] Y. Du, H. Liu, Cage-like Silsesquioxanes-Based Hybrid Materials, Dalton Transactions 49 (2020) 5396–5405, https://doi.org/10.1039/D0DT00587H.
[30] M.G. Mohamed, S.W. Kuo, Progress in the self-assembly of organic/inorganic polyhedral oligomeric silsesquioxane (POSS) hybrids, Soft Matter 18 (2022) 5535–5561, https://doi.org/10.1039/D2SM00635A.
[31] X. Lin, Y.Y. Deng, Q. Zhang, D. Han, Q. Fu, Effect of POSS size on the porosity and adsorption performance of hybrid porous polymers, Macromolecules 56 (2023) 1243, https://doi.org/10.1021/acs.macromol.2c02486.
[32] C.Y. Chen, W.C. Chen, M.G. Mohamed, Z.Y. Chen, S.W. Kuo, Highly thermally stable, reversible and flexible main chain-type benzoxazine hybrid incorporating both polydimethylsiloxane and double-decker–shaped polyhedral silsesquioxane, Macromolecular Rapid Communications 44 (2023) 2200910, https://doi.org/10.1002/marc.202200910.
[33] S. Takase, T. Hamada, K. Okada, S. Mineoi, J. Ohshita, Polysilsesquioxane-containing thermally degradable groups for potential application as thermal insulation materials, ACS Appl. Polym. Mater. 5 (2023) 1390, https://doi.org/10.1021/acsapm.2c01900.
[34] D.L. Zhou, X. Wang, W.C. Qu, Q.Y. Guo, C.Y. Li, Q. Zhang, D. Han, Q. Fu, Linker engineering of larger POSS-based ultra-low-k dielectrics toward outstanding comprehensive properties, Giant 14 (2023), 100146, https://doi.org/10.1016/j.giant.2023.100146.
[35] C.H. Chiang, M.G. Mohamed, W.C. Chen, M. Madhu, W.L. Tseng, S.W. Kuo, Construction of fluorescent conjugated polytriazole containing double-decker silsesquioxane: Click polymerization and thermal stability, Polymers 15 (2023) 331, https://doi.org/10.3390/polym15020331.
[36] X. Wang, B. Liu, D. Chen, D. Zhang, X. Li, J. He, R. Yang, Molecular-level fabrication strategies for the POSS cross-linked polybenzoxazines, Journal of Polymer Science 61 (2023) 1634, https://doi.org/10.1002/pol.20230052.
[37] W. Li, H. Liu, Novel organic–inorganic hybrid polymer based on fluorinated polyhedral oligomeric silsesquioxanes for stable superamphiphobic fabrics and aluminum corrosion protection, Materials Today Chemistry 29 (2023), 101390, https://doi.org/10.1016/j.mtchem.2023.101390.
[38] M.G. Mohamed, S.W. Kuo, Functional silica and carbon nanocomposites based on polybenzoxazines, Macromolecular Chemistry and Physics 220 (2019) 1800306, https://doi.org/10.1002/macp.201800306.

[39] M.G. Mohamed, S.W. Kuo, Functional polyimide/polyhedral oligomeric silsesquioxane nanocomposites, Polymers 11 (2019) 26, https://doi.org/10.3390/polym11010026.
[40] D. Zhang, J. Zeng, S. Zhu, H. Ma, X. Kang, L. Lou, Z. He, Effects of polyhedral oligomeric silsesquioxane and silicon microstructure on the electric-optical performance of polymer dispersed liquid crystals, Optical Materials 140 (2023), 113877, https://doi.org/10.1016/j.optmat.2023.113877.
[41] Y. Yan, H. Yang, H. Liu, Silsesquioxane-based fluorescent nanoporous polymer derived from a novel AIE chromophore for concurrent detection and adsorption of Ru^{3}+, Sensors and Actuators B: Chemical 319 (2020), 128154 https://doi.org/10.1016/j.snb.2020.128154.
[42] Z. Chen, D. Wang, S. Feng, H. Liu, an imidazole thione-modified polyhedral oligomeric silsesquioxane for selective detection and adsorptive recovery of Au (III) from aqueous solutions, ACS Applied Materials & Interfaces 13 (2021) 23592–23605, https://doi.org/10.1021/acsami.1c01965.
[43] S. Mahbub, S. Saha, G. Ramakrishna, J.C. Furgal, Beads on a chain fluorescent oligomeric materials: Interactions of conjugated organic cross-linkers with silsesquioxane cages, The Journal of Physical Chemistry. B 125 (2021) 11457–11472.
[44] M. Ejaz, M.M. Samy, Y. Ye, S.W. Kuo, M.G. Mohamed, Design hybrid porous organic/inorganic polymers containing polyhedral oligomeric silsesquioxane/pyrene/anthracene moieties as a high-performance electrode for supercapacitor, International Journal of Molecular Sciences 24 (2023) 2501, https://doi.org/10.3390/ijms24032501.
[45] M.G. Mohamed, M.H. Elsayed, Y. Ye, M.M. Samy, A.E. Hassan, T.H. Mansoure, Z. Wen, H.H. Chou, K.H. Chen, S.W. Kuo, Construction of porous organic/inorganic hybrid polymers based on polyhedral oligomeric silsesquioxane for energy storage and hydrogen production from water, Polymers 15 (2023) 182, https://doi.org/10.3390/polym15010182.
[46] Q. Wang, M. Unno, H. Liu, Organic−inorganic hybrid near-infrared emitting porous polymer for detection and photodegradation of antibiotics, ACS Sustainable Chemistry & Engineering 10 (2022) 7309–7320, https://doi.org/10.1021/acssuschemeng.2c00935.
[47] Z. Wang, R. Kunthom, S.V. Kostjuk, H. Liu, Near-infrared-emitting silsesquioxane-based porous polymer containing thiophene for highly efficient adsorption and detection of iodine vapor and solution phase, Eur. P. J. 192 (2023) 112072, https://doi.org/10.1016/j.eurpolymj.2023.112072.
[48] Z. Wang, A. Mathew, H. Li, Silsesquioxane-based porous polymer derived from organic chromophore with AIE characteristics for selective detection of 2,4-dinitrophenol and Ru^{3}+, Polymer 248 (2022), 124788 https://doi.org/10.1016/j.polymer.2022.124788.
[49] Q. Wang, M. Unno, H. Liu, Silsesquioxane-based triphenylamine-linked fluorescent porous polymer for dyes adsorption and nitro-aromatics detection, Materials 14 (14) (2021) 3851, https://doi.org/10.3390/ma14143851.
[50] M.G. Mohamed, M.-Y. Tsai, C.-F. Wang, C.-F. Huang, M. Danko, L. Dai, T. Chen, S.-W. Kuo, Multifunctional polyhedral oligomeric silsesquioxane (POSS) based hybrid porous materials for CO2 uptake and iodine adsorption, Polymers 13 (2021) 221, https://doi.org/10.3390/polym13020221.
[51] M.G. Mohamed, T.H. Mansoure, Y. Takashi, M.M. Samy, T. Chen, S.W. Kuo, Ultrastable porous organic/inorganic polymers based on polyhedral oligomeric silsesquioxane (POSS) hybrids exhibiting high performance for thermal property and energy storage, Microporous and Mesoporous Materials 328 (2021), 111505, https://doi.org/10.1016/j.micromeso.2021.111505.
[52] Y. Yan, R.M. Laine, H. Liu, In situ methylation transforms aggregation-caused quenching into aggregation-induced emission: Functional porous silsesquioxane-based composites with enhanced near-infrared emission, ChemPlusChem 84 (2019) 1630–1637, https://doi.org/10.1002/cplu.201900568.
[53] Y. Liu, Y. Li, S. Koo, Y. Sun, Y. Liu, X. Liu, Y. Pan, Z. Zhang, M. Du, S. Lu, X. Qing, J. Gao, X. Wang, Z. Deng, X. Meng, Y. Xiao, J.S. Kim, X. Hong, Versatile types of inorganic/organic NIR-IIa/IIb fluorophores: From strategic design toward molecular imaging and theranostics, Chemical Reviews 122 (2022) 209–268, https://doi.org/10.1021/acs.chemrev.1c00553.
[54] A. Alam, A. Hassan, R. Bera, N. Das, Silsesquioxane-based and triptycene-linked nanoporous polymers (STNPs) with a high surface area for CO2 uptake and efficient dye removal applications, Mater. Adv. 1 (2020) 3406–3416, https://doi.org/10.1039/D0MA00672F.
[55] M. Ejaz, M.G. Mohamed, S.U. Sharma, J.T. Lee, C.F. Huang, T. Chen, S.W. Kuo, An ultrastable porous polyhedral oligomeric silsesquioxane/tetraphenylthiophene hybrid as a high-performance electrode for supercapacitors, Molecules 27 (2022) 6238, https://doi.org/10.3390/molecules27196238.
[56] Y. Wang, M. Soldatov, Q. Wang, H. Liu, Phosphazene functionalized silsesquioxane-based porous polymers for absorbing I_2, CO_2 and dyes, Polymer 218 (2021), 123491, https://doi.org/10.1016/j.polymer.2021.123491.
[57] Y. Zhang, N. Luo, J. Xu, K. Liu, S. Zhang, Q. Xu, R. Huang, Z. Long, M. Tong, G. Chen, Metalated-bipyridine-based porous hybrid polymers with POSS-derived Si–OH groups for synergistic catalytic CO_2 fixation, Dalton Transactions 49 (2020) 11300–11309, https://doi.org/10.1039/D0DT01667E.
[58] Y. Zhang, K. Liu, L. Wu, H. Huang, Z. Xu, Z. Long, M. Tong, Y. Gu, Z. Qin, G. Chen, POSS and imidazolium-constructed ionic porous hypercrosslinked polymers with multiple active sites for synergistic catalytic CO_2 transformation, Dalton Transactions 50 (2021) 11878–11888, https://doi.org/10.1039/D1DT02067F.
[59] H. Huang, C. Meng, Z. Xu, S.W.Y. Chang, S. Wang, J. Chen, Z. Long, G. Chen, Construction of silsesquioxane and phosphinum-based ionic porous hypercrosslinked polymers for efficient heterogeneous catalytic CO2 cycloaddition, J. Poly. Sci. (2023), https://doi.org/10.1002/pol.20230335.
[60] G. Chen, X. Huang, Y. Zhang, M. Sun, J. Shen, R. Huang, M. Tong, Z. Long, X. Wang, Constructing POSS and viologen-linked porous cationic frameworks induced by the Zincke reaction for efficient CO_2 capture and conversion, Chemical Communications 54 (2018) 12174–12177, https://doi.org/10.1039/C8CC06972G.
[61] M.G. Mohamed, M.M.M. Ahmed, W.-T. Du, S.-W. Kuo, Meso/microporous carbons from conjugated hyper-crosslinked polymers based on tetraphenylethene for high performance for CO_2 capture and supercapacitor, Molecules 26 (2021) 738, https://doi.org/10.3390/molecules26030738.
[62] T.H. Weng, M.G. Mohamed, S.U. Sharma, S.V. Chaganti, M.M. Samy, J.T. Lee, S. W. Kuo, Ultrastable three-dimensional triptycene- and tetraphenylethene-conjugated microporous polymers for energy storage, ACS Appl. Energy Mater. 5 (2022) 14239–14249, https://doi.org/10.1021/acsaem.2c02809.
[63] M.G. Mohamed, S.U. Sharma, C.H. Yang, M.M. Samy, A.A.K. Mohammed, S. V. Chaganti, J.T. Lee, S.W. Kuo, Anthraquinone-enriched conjugated microporous polymers as organic cathode materials for high-performance lithium-ion batteries, ACS Appl. Energy Mater. 4 (2021) 14628–14639, https://doi.org/10.1021/acsaem.1c03270.
[64] M.M. Samy, M.G. Mohamed, S.U. Sharma, S.V. Chaganti, J.T. Lee, S.W. Kuo, An ultrastable tetrabenzonaphthalene-linked conjugated microporous polymer functioning as a high-performance electrode for supercapacitors, Journal of the Taiwan Institute of Chemical Engineers (2023), 104750, https://doi.org/10.1016/j.jtice.2023.104750.
[65] M.G. Mohamed, W.C. Chang, S.W. Kuo, Crown ether- and benzoxazine-linked porous organic polymers displaying enhanced metal ion and CO_2 capture through solid-state chemical transformation, Macromolecules 55 (2022) 7879–7892, https://doi.org/10.1021/acs.macromol.2c01216.
[66] M.G. Mohamed, T.C. Chen, S.W. Kuo, Solid-state chemical transformations to enhance gas capture in benzoxazine-linked conjugated microporous polymers, Macromolecules 54 (2021) 5866–5877, https://doi.org/10.1021/acs.macromol.1c00736.
[67] M.G. Mohamed, M.H. Elsayed, A.M. Elewa, A.F.M. El-Mahdy, C.H. Yang, A.A. K. Mohammed, H.H. Chou, S.W. Kuo, Pyrene-containing conjugated organic microporous polymers for photocatalytic hydrogen evolution from water, Catalysis Science & Technology 11 (2021) 2229–2241, https://doi.org/10.1039/D0CY02482A.
[68] A.V. Deshpande, U. Kumar, Effect of method of preparation on photophysical properties of Rh-B impregnated sol–gel hosts, Journal of Non-Crystalline Solids 306 (2002) 149–159, https://doi.org/10.1016/S0022-3093(02)01054-2.
[69] M.R. Mahmoud, G.M. Rashad, A.M. Elewa, E. Metwally, E.A. Saad, Optimization of adsorption parameters for removal of 152+154Eu(III) from aqueous solutions by using Zn-Cu-Ni ternary mixed oxide, Journal of Molecular Liquids 291 (2019) 11125, https://doi.org/10.1016/j.molliq.2019.111257.